Sigmoid-Function-Based Feedback Linearization Random Selection Control for Cascaded H-Bridge Multilevel Inverters

Zhihong Yin and Yimin Lu, *Member, IEEE*

***Abstract*—To improve the steady-state and dynamic performance of cascaded H-bridge multilevel inverters (CHBMIs) and achieve power balance, this article proposes a control method based on the sigmoid function that combines feedback linearization with a random selection strategy. First, a continuous-smooth sigmoid function model that can uniformly describe all switching-state combinations is established. Subsequently, the control law is derived by applying the feedback linearization theory. The output levels are determined based on the control law and the characteristics of the sigmoid function. Finally, the desired switching-state combinations are determined through two random selections and applied directly to the switching devices. The proposed method is not only applicable to symmetric CHBMIs but also applicable to asymmetric CHBMIs. Simulations and experimental verifications are carried out on the control systems of a symmetric CHBMI with a linear load and an asymmetric CHBMI with a nonlinear load, and comparisons are made with other methods. The results show that the proposed method exhibits better steady-state and dynamic performance, achieving a higher power balance degree, and is suitable for both symmetric and asymmetric CHBMIs.**

***Index Terms*—Cascaded H-bridge multilevel inverters (CHBMIS), feedback linearization, random selection, sigmoid function model.**

I. Introduction

CASCADED H-bridge multilevel inverter (CHBMI) is one of the most popular multilevel inverter topologies, due to its modularity, scalability, and fault-tolerant capability [1], [2]. According to whether the dc-side voltages are equal, CHBMIs can be divided into symmetric CHBMIs and asymmetric CHBMIs [3]. Among them, asymmetric CHBMIs can generate more levels under the condition of the same number of inverter units, but their control complexity is higher. Nowadays, CHBMIs have been widely used in several fields, such as energy storage and renewable energy systems [4], [5], [6], [7], [8]. As a critical component, the CHBMI's performance significantly impacts overall system operation. Consequently, CHBMIs are required to exhibit excellent steady-state and dynamic performance. Furthermore, as each inverter unit in CHBMIs provides active power independently, it is essential to ensure balanced power distribution among all inverter units. Power imbalance can cause lifespan disparities in dc-side components, compromising reliability and increasing maintenance costs [9]. Thus, investigating control methods that enable CHBMIs to achieve excellent steady-state and dynamic performance, and power balance, is of significant importance.

Linear control strategies based on pulse width modulation (PWM), such as proportional-integral (PI) control [10] or proportional-resonant control [11], have been widely applied in multilevel converters, including CHBMIs. Due to the presence of multiple switching devices in CHBMIs, multicarrier PWM is required. Multicarrier PWM can be primarily categorized into phase-shifted PWM (PS-PWM) and level-shifted PWM (LS-PWM). Compared with PS-PWM, LS-PWM has better output voltage harmonic performance, but it cannot achieve power balance among inverter units [12]. In study [13], a carrier rotation LS-PWM (CR-LS-PWM) was proposed to compensate for the deficiency that LS-PWM cannot achieve power balance. However, CR-LS-PWM and PS-PWM are only suitable for symmetric CHBMIs and not for asymmetric CHBMIs. On one hand, these two methods are difficult to ensure power balance between high- and low-voltage inverter units; on the other hand, it is difficult to ensure that high-voltage units operate in a low-frequency state to reduce the loss of switching devices. In [14], a power balance improved hybrid modulation PWM (PBIH-PWM) was proposed to achieve the power balance of asymmetric CHBMIs and ensure that the high-voltage unit operates in a low-frequency state. However, Ye et al. [14] only studied open-loop control and did not conduct closed-loop control research. In addition, when the number of inverter units increases significantly, multiple distinct carrier signals need to be generated simultaneously. Owing to the limited parallel processing capabilities of digital signal processor (DSPs), it becomes challenging to meet the requirements for real-time performance and control accuracy, necessitating the use of costly field programmable gate array (FPGA) [15]. Although linear control based on PWM offers advantages such as simplicity in implementation and ease of tuning control parameters, the CHBMI system is highly nonlinear with a wide range of operational points. As a result, the dynamic performance of linear control is not satisfactory.

Received 3 November 2025; accepted 1 January 2026. Date of publication 12 January 2026; date of current version 20 March 2026. This work was supported in part by the National Natural Science Foundation of China under Grant 52167021 and in part by the Innovation Project of Guangxi Graduate Education under Grant YCBZ2023044. Recommended for publication by Associate Editor I. Tsoumas. *(Corresponding author: Yimin Lu.)*

The authors are with the School of Electrical Engineering, Guangxi University, Nanning 530004, China (e-mail: 2212401008@st.gxu.edu.cn; y.m.lu@gxu.edu.cn).

Color versions of one or more figures in this article are available at https://doi.org/10.1109/TPEL.2026.3652248.

Digital Object Identifier 10.1109/TPEL.2026.3652248

Due to its good steady-state and dynamic performance, finite control set model predictive control (FCS-MPC) has emerged as another widely used control strategy for multilevel converters [16]. However, when FCS-MPC is applied to CHBMIs, achieving power balance poses significant challenges. This is because implementing power balance by introducing multiple custom constraints into the cost function not only requires sampling the output voltages of each inverter unit but also necessitates continuous adjustment of multiple weighting factors, which is a cumbersome trial-and-error process. This approach not only increases control complexity but may also adversely affect system performance [17]. Furthermore, the number of switching-state combinations of the CHBMIs increases exponentially as the number of inverter units increases [18]. This dramatically increases the computational burden. In studies [19], [20], [21], [22], and [23], FCS-MPC was improved by using output voltage levels as optimization variables, reducing the number of switching-state combinations in the control set, or performing offline pre-calculations, significantly reducing the computational burden of the algorithm. Nevertheless, the studies mentioned above have not effectively solved the power balance problem of the system. In addition, for asymmetric CHBMIs, FCS-MPC also has difficulty ensuring that its high-voltage unit operates in a low-frequency state.

In summary, to ensure the power balance of CHBMIs while maintaining good steady-state and dynamic performance, a feedback linearization random selection control method based on the sigmoid function is proposed. The sigmoid function with a large steepness factor can be employed to describe the switching process of power devices, as its values asymptotically approach either 0 or 1. In studies [24] and [25], the sigmoid function was utilized for modeling resonant converters. The results demonstrated that, compared to other models, the sigmoid function model offers a simpler modeling process, provides a more accurate description of the converter's operational characteristics, and possesses the advantage of being continuous and smooth. This lays the foundation for designing controllers based on continuous-system nonlinear control theory. However, in published works, the sigmoid function has only been used for the modeling and dynamics analysis of the converter, and has not been used for the design of the converter control strategy. In this article, the sigmoid function is used to combine the nonlinear control theory of the continuous system with the random selection strategy, and a control method for the CHBMI is proposed. The main contributions of this article are as follows.

1) A continuous-smooth sigmoid function model for CHBMIs is established, which facilitates the design of control laws in conjunction with continuous-system nonlinear control theory.
2) Based on the sigmoid function model, the feedback linearization theory is applied to design the control law, ensuring excellent steady-state and dynamic performance.
3) Based on the control law and the sigmoid function, a unique switching-state combination is determined through two random selections, achieving power balance.

The remainder of this article is organized as follows: Section II describes the circuit structure and switching-state combinations of the CHBMI containing N inverter units; Section III takes the symmetric CHBMI as an example, introduces in detail the steps and principle of the proposed method; Sections IV extends the proposed method to the asymmetric CHBMI; Sections V and VI respectively give the simulation and experimental comparison results between the proposed method and the existing methods. Section VII concludes this article.

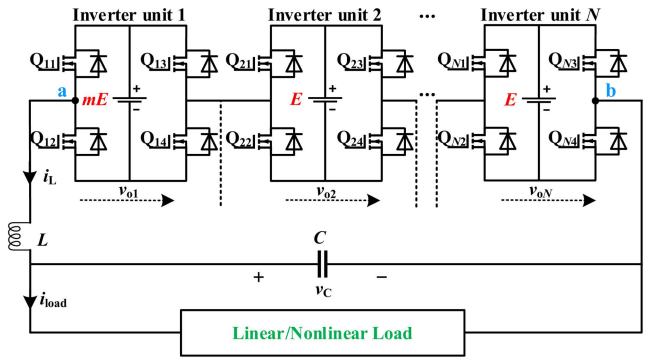

Fig. 1. Circuit structure of the CHBMI containing N units.

II. Circuit Structure and Switching-State Combinations of CHBMIs Containing N Units

The structure of a CHBMI consisting of N H-bridge inverter units is shown in Fig. 1. The dc-side voltage of unit 1 is mE, and the dc-side voltages of units $2-N$ are all E. When $m = 1$, the CHBMI is symmetric, and its dc-side voltage ratio is 1: 1: ⋯: 1. When $m > 1$ (m is a positive integer and $m \leq N-1$), unit 1 is a high-voltage unit, units $2-N$ are all low-voltage units, and the CHBMI is asymmetric, with its dc-side voltage ratio m: 1: ⋯: 1. The $2N$ bridge arms are composed of switching devices Q_{i1}–Q_{i4} ($i = 1, 2, \ldots, N$) with anti-parallel diodes. An LC circuit is used for filtering. For generality, the load can be either linear or nonlinear. v_{oi} is the output voltage of the ith unit, v_{ab} is the output voltage of the CHBMI inverter bridge. i_L, i_{load}, and v_C are the inductor current, load current, and capacitor voltage (load voltage), respectively. The discrete switching variables q_{i1} and q_{i2} are defined to describe the states of switching devices $Q_{i1}-Q_{i4}$. When Q_{i1} is on and Q_{i2} is OFF, $q_{i1} = 1$; while when Q_{i1} is OFF and Q_{i2} is ON, $q_{i1} = 0$. When Q_{i4} is ON and Q_{i3} is OFF, $q_{i2} = 1$; while when Q_{i4} is OFF and Q_{i3} is ON, $q_{i2} = 0$.

The four switching-state combinations of any ith inverter unit are combination 1: $q_{i1} = 1$, $q_{i2} = 1$, $Q_{i1}Q_{i4}$ on, $Q_{i2}Q_{i3}$ OFF, $v_{oi} = E$; combination 2: $q_{i1} = 1, q_{i2} = 0$, $Q_{i1}Q_{i3}$ on, $Q_{i2}Q_{i4}$ OFF, $v_{oi} = 0$; combination 3: $q_{i1} = 0, q_{i2} = 1$, $Q_{i2}Q_{i4}$ on, $Q_{i1}Q_{i3}$ OFF, $v_{oi} = 0$; combination 4: $q_{i1} = 0$, $q_{i2} = 0$, $Q_{i2}Q_{i3}$ on, $Q_{i1}Q_{i4}$ OFF, $v_{oi} = -E$. To distinguish between the two combinations producing 0, the state where $Q_{i1}Q_{i3}$ are ON and $Q_{i2}Q_{i4}$ are OFF is represented as the numeral "1," whereas the state where $Q_{i2}Q_{i4}$ are ON and $Q_{i1}Q_{i3}$ are OFF is represented as the numeral "2." Therefore, a CHBMI with N units has 4^N switching-state combinations. A symmetric CHBMI has $2N + 1$ different output levels, whereas an asymmetric CHBMI has a maximum of $4N - 3$. Except for the highest and lowest levels, the remaining

TABLE I
SWITCHING-STATE COMBINATIONS OF SYMMETRIC CHBMI CORRESPONDING TO EACH OUTPUT LEVEL

Output voltage v_{ab}	Switching-state combination $q_{11}q_{12}q_{21}q_{22}\cdots q_{N1}q_{N2}$	Quantity of combinations
NE	$1111\cdots11$	C($2N$, 0)
$(N–1)E$	$0111\cdots11$ $1011\cdots11$ $\vdots$ $1111\cdots10$	C($2N$, 1)
$\vdots$	$\vdots$	$\vdots$
$–(N–1)E$	$1000\cdots00$ $0100\cdots00$ $\vdots$ $0000\cdots01$	C($2N$, $2N$–1)
$–NE$	$0000\cdots00$	C($2N$, $2N$)

TABLE II
SWITCHING-STATE COMBINATIONS OF ASYMMETRIC CHBMI CORRESPONDING TO EACH OUTPUT LEVEL

Output voltage v_{ab}	Switching-state combination $q_{11}q_{12}q_{21}q_{22}\cdots q_{N1}q_{N2}$	Quantity of combinations
$(N–1+m)E$	$1111\cdots11$	C($2N$, 0)
$(N–2+m)E$	$1101\cdots11$ $1110\cdots11$ $\vdots$ $1111\cdots10$	C($2N$, 1) – 2
$\vdots$	$\vdots$	$\vdots$
$–(N–2+m)E$	$0010\cdots00$ $0001\cdots00$ $\vdots$ $0000\cdots01$	C($2N$, $2N$–1) – 2
$–(N–1+m)E$	$0000\cdots00$	C($2N$, $2N$)

output levels all correspond to multiple switching-state combinations. The corresponding switching-state combinations and their quantities for each output level of symmetric and asymmetric CHBMIs are listed in Tables I and II, respectively.

III. PROPOSED CONTROL METHOD

Fig. 2 outlines the design process of the proposed control method, which comprises four steps.

In this section, a symmetric CHBMI with N inverter units is used as an example to detail the steps and control principle of the proposed method. In Section IV, the proposed method is extended to asymmetric CHBMIs.

A. Sigmoid Function Model of Symmetric CHBMI Containing N Units

In power electronic converters with negative feedback control, switching-state combinations are typically determined dynamically based on the feedback values of current and voltage. Therefore, it may be assumed that the values of discrete switching variables q_{i1} and q_{i2} of the symmetric CHBMI (as shown in Fig. 1, $m = 1$) are determined by the continuous functions $f_{i1}(i_L, v_C)$, $f_{i2}(i_L, v_C)$. The specific switching control logic of each unit is as follows: when $f_{i1}(i_L, v_C) > 0$, $q_{i1} = 1$; when $f_{i1}(i_L, v_C) < 0$, $q_{i1} = 0$; when $f_{i2}(i_L, v_C) > 0$, $q_{i2} = 1$; when $f_{i2}(i_L, v_C) < 0$, $q_{i2} = 0$. Thus, the relationship between $f_{i1/i2}(i_L, v_C)$ and $q_{i1/i2}$ can be described using the step function H

$$q_{i1/i2} = H\left(f_{i1/i2}\left(i_L, v_C\right)\right) = \begin{cases} 1, & f_{i1/i2}\left(i_L, v_C\right) > 0 \\ 0, & f_{i1/i2}\left(i_L, v_C\right) < 0 \end{cases}. \quad (1)$$

v_{ab} can be expressed as follows:

$$v_{ab} = \psi E \quad (2)$$

where $\psi = \sum_{i=1}^{N}(q_{i1} + q_{i2}) - N$.

Equation (2) is a segmented smooth expression containing singular functions. To facilitate controller design using the continuous-system theory, q_{i1} and q_{i2} in (2) are replaced by a sigmoid function containing a large steepness factor a to make the model smooth

$$v_{ab} \approx \left(\sum_{i=1}^{N}\left(S\left(af_{i1}\left(i_L, v_C\right)\right) + S\left(af_{i2}\left(i_L, v_C\right)\right)\right) - N\right)E$$

$$= \sum_{i=1}^{N}\left(\frac{1}{1+\exp\left(-af_{i1}\left(i_L, v_C\right)\right)} + \frac{1}{1+\exp\left(-af_{i2}\left(i_L, v_C\right)\right)}\right)E - NE. \quad (3)$$

Consequently, a unified continuous-smooth sigmoid function model describing all the switching-state combinations of the symmetric CHBMI can be established

$$\begin{cases} \dot{\mathbf{x}} = \boldsymbol{f}\left(\mathbf{x}\right) + \boldsymbol{g}\left(\mathbf{x}\right)u \\ \mathbf{y} = \mathbf{h}\left(\mathbf{x}\right) \end{cases} \quad (4)$$

where $\mathbf{x} = [x_1, x_2, \ldots, x_n]^T$, $\boldsymbol{f}(\mathbf{x}) = [f_1(\mathbf{x}), f_2(\mathbf{x}), \ldots, f_n(\mathbf{x})]^T$, $\boldsymbol{g}(\mathbf{x}) = [g_1(\mathbf{x}), g_2(\mathbf{x}), \ldots, g_n(\mathbf{x})]^T$, $\mathbf{y} = [y_1, y_2]^T = [h_1(x), h_2(x)]^T = [v_C, i_L]^T$, $u = v_{ab}/E$. As shown in Fig. 1, $x_1 = i_L$, $x_2 = v_C$; $f_1(\mathbf{x}) = -v_C/L$, $f_2(\mathbf{x}) = i_L/C - v_C/(R_L C)$; $g_1(\mathbf{x}) = E/L$, $g_2(\mathbf{x}) = 0$. $x_3 - x_n$, $f_3(\mathbf{x}) - f_n(\mathbf{x})$, and $g_3(\mathbf{x}) - g_n(\mathbf{x})$ are all determined by the load carried. Whether it is a linear or nonlinear load, its control objective is to ensure that v_C and i_{load} track the given reference values. And i_{load} is determined by v_C and i_L. Therefore, the output functions $h_1(x) = v_C$, $h_2(x) = i_L$ are selected.

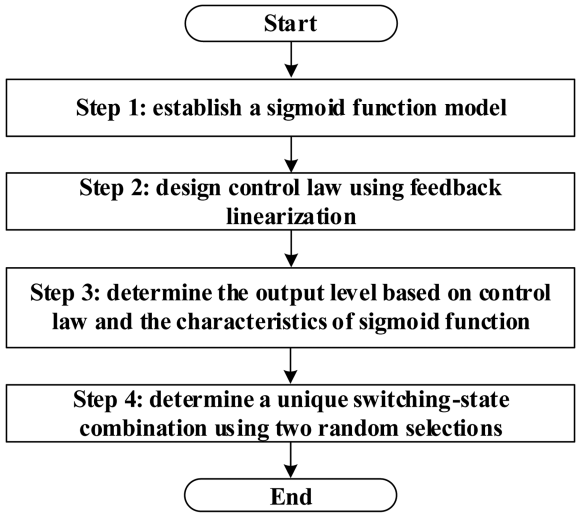

Fig. 2. Design flowchart of the proposed control method.

B. Design of Control Law and Analysis of Control Principles

The controller designed using the feedback linearization method exhibits excellent steady-state and dynamic performance [26]. Therefore, based on the sigmoid function model (4), the control law is designed by using the feedback linearization method. Commonly used feedback linearization methods, such as differential geometry and inverse system theory, require the system inputs and outputs to be of the same dimension when designing control laws. Otherwise, it is difficult to ensure that all output quantities achieve tracking control [27]. In addition, to achieve fully exact linearization, it is necessary to satisfy the condition that the relative order of the output function is equal to the system dimension. However, model (4) is a single-input, dual-output system, and its input and output dimensions are not equal. Moreover, the system dimension is related to the load type. When the load changes, it is difficult to ensure that the relative order of the output function is equal to the system dimension. Therefore, the commonly used feedback linearization methods are not applicable to system (4).

In study [27], an improved feedback linearization method was proposed. This method actively constructs the Brunovsky canonical form by using the deviation equation between the output quantity and the reference output quantity, and transforms the nonlinear system into a linear system. This method does not need to satisfy the harsh conditions that the input and output dimensions are equal, and the relative order of the output function is equal to the system dimension. It only needs that there is a relative order of 1 for one component of the output function to ensure that all outputs achieve tracking control. For system (4), in the neighborhood of the equilibrium point $\mathbf{x_e}$, the output function component $y_2 = h_2(x)$ satisfies the following:

$$L_g L_f^0 h_2(x) = \frac{E}{L} \neq 0. \tag{5}$$

$h_2(x)$ has a relative degree of 1; hence, the feedback linearization method in study [27] can be applied to design the control law u such that the deviation equations in (6) satisfy (7)

$$I_l = y_l - y_{l\text{ref}} \, (l = 1, 2) \tag{6}$$

$$\lim_{t\to\infty} |I_l| = 0. \tag{7}$$

First, from (4)

$$\dot{y}_2 = L_f h_2(x) + L_g L_f^0 h_2(x)\, u \tag{8}$$

where $L_f h_2(x) = -v_C/L$. Subsequently, the tracking deviation I_l in (6) is used to form the dynamic equation system, which is written in the second-order Brunovsky canonical form

$$\dot{\mathbf{I}} = \mathrm{A}\mathbf{I} + \mathbf{B}v \tag{9}$$

where $\mathbf{I} = \begin{bmatrix} I_1 \\ I_2 \end{bmatrix} = \begin{bmatrix} y_1 - y_{1\text{ref}} \\ y_2 - y_{2\text{ref}} \end{bmatrix}$, $\mathbf{A} = \begin{bmatrix} 0 & 1 \\ 0 & 0 \end{bmatrix}$, $\mathbf{B} = \begin{bmatrix} 0 \\ 1 \end{bmatrix}$

$$v = \dot{y}_2 - \dot{y}_{2\text{ref}} = L_f h_2(x) + L_g L_f^0 h_2(x)\, u - \dot{y}_{2\text{ref}}. \tag{10}$$

System (9) is a fully controllable linear system, and its feedback control law can be obtained by using the optimal control method:

$$v = -k_1 I_1 - k_2 I_2. \tag{11}$$

Substituting (11) into (10) provides the input control law for system (4):

$$u = \left[-k_1 I_1 - k_2 I_2 - L_f h_2(x) + \dot{y}_{2\text{ref}}\right] / L_g L_f^0 h_2(x) \tag{12}$$

where k_1 and k_2 are the control parameters. The following introduces the control principle and the design basis of k_1 and k_2. According to the Hartman-Grobman theorem [28], in the neighborhood of the hyperbolic equilibrium point of the nonlinear system, as long as its first-order approximation system is stable, the nonlinear system is also stable. Therefore, the same control law is applied to the first-order approximation system of (4), and the control coefficients are designed by configuring its poles. Perform Taylor expansion on system (4) at the equilibrium point $\mathbf{x_e}$, and ignore the high-order terms to obtain its first-order approximation system

$$\begin{cases} \dot{\mathbf{x}}_\mathbf{o} = \mathbf{A_o}\mathbf{x_o} + \mathbf{B_o}u_\mathrm{o} \\ \mathbf{y_o} = \mathbf{C_o}\mathbf{x_o} \end{cases} \tag{13}$$

where $\mathbf{x_o}$ is an n-dimensional state column vector; $\mathbf{A_o}$ is an $n\times n$ matrix; $\mathbf{B_o}$ is an $n\times 1$ matrix; $\mathbf{C_o}$ is a $2\times n$ matrix; u_o is a control scalar; and $\mathbf{y_o}$ is a control objective. Assume that $\mathbf{x_{oref}}$ and $\mathbf{y_{oref}}$ are the references of $\mathbf{x_o}$ and $\mathbf{y_o}$. There always exists a reference control law u_{oref} such that $\mathbf{x_{oref}}$ and $\mathbf{y_{oref}}$ satisfy (13). Select a linear nonsingular matrix $\mathbf{T_s}$, perform linear transformations $\mathbf{x_s} = \mathbf{T_s}\mathbf{x_o}$ and $\mathbf{x_{sref}} = \mathbf{T_s}\mathbf{x_{oref}}$, and transform (13) into the controllable canonical form

$$\begin{cases} \dot{\mathbf{x}}_\mathbf{s} = \mathbf{A_s}\mathbf{x_s} + \mathbf{B_s}u_\mathrm{o} \\ \mathbf{y_s} = \mathbf{C_s}\mathbf{x_s} \end{cases} \tag{14}$$

where

$$\mathbf{A}_\mathrm{s} = \begin{bmatrix} 0 & 1 & 0 & \cdots & 0 \\ 0 & 0 & 1 & \cdots & 0 \\ \vdots & \vdots & \vdots & \vdots & \vdots \\ 0 & 0 & 0 & \cdots & 1 \\ -a_0 & -a_1 & -a_2 & \cdots & -a_{n-1} \end{bmatrix}$$

$\mathbf{C_s} = \mathbf{C_o}\mathbf{T_s^{-1}} = \begin{bmatrix} \mathbf{C_{s1}} \\ \mathbf{C_{s2}} \end{bmatrix} = \begin{bmatrix} c_{11} & c_{12} & c_{13} & \cdots & c_{1n} \\ c_{21} & c_{22} & c_{23} & \cdots & c_{2n} \end{bmatrix}$, $\mathbf{B_s} = [0, 0, 0, \ldots, 1]^\mathrm{T}$. Assume that there exist $\mathbf{x_{sref}}$ and $\mathbf{y_{sref}}$ satisfying (14), then we can obtain

$$\begin{cases} \dot{\mathbf{x}}_{\mathrm{sref}} = \mathbf{A}_\mathrm{s}\mathbf{x_{sref}} + \mathbf{B}_\mathrm{s}u_{\mathrm{oref}} \\ \mathbf{y}_{\mathrm{sref}} = \mathbf{C}_\mathrm{s}\mathbf{x}_{\mathrm{sref}} \end{cases}. \tag{15}$$

For the linear system (14), the relative order of the output quantity $y_{\mathrm{s}2}$ to this system is 1, and we can obtain

$$\dot{y}_{\mathrm{s}2} = \frac{\partial y_{\mathrm{s}2}}{\partial \mathbf{x}_\mathrm{s}}\dot{\mathbf{x}}_\mathrm{s} = \mathbf{C}_{\mathrm{s}2}\mathbf{A}_\mathrm{s}\mathbf{x}_\mathrm{s} + \mathbf{C}_{\mathrm{s}2}\mathbf{B}_\mathrm{s}u_\mathrm{o}. \tag{16}$$

The reference trajectory $y_{\mathrm{s}2\mathrm{ref}}$ of $y_{\mathrm{s}2}$ satisfies

$$\dot{y}_{\mathrm{s}2\mathrm{ref}} = \frac{\partial y_{\mathrm{s}2\mathrm{ref}}}{\partial \mathbf{x_{sref}}}\dot{\mathbf{x}}_{\mathrm{sref}} = \mathbf{C}_{\mathrm{s}2}\mathbf{A}_\mathrm{s}\mathbf{x_{sref}} + \mathbf{C}_{\mathrm{s}2}\mathbf{B}_\mathrm{s}u_{\mathrm{oref}}. \tag{17}$$

For system (14), the control law is adopted

$$u_\mathrm{o} = (\mathbf{C_{s2}}\mathbf{B_s})^{-1}\left[-k_{\mathrm{s}1}\left(y_{\mathrm{s}1} - y_{\mathrm{s}1\mathrm{ref}}\right) - k_{\mathrm{s}2}\left(y_{\mathrm{s}2} - y_{\mathrm{s}2\mathrm{ref}}\right)\right] - (\mathbf{C_{s2}}\mathbf{B_s})^{-1}\left(\mathbf{C_{s2}}\mathbf{A_s}\mathbf{x_s} - \dot{y}_{\mathrm{s}2\mathrm{ref}}\right). \tag{18}$$

Substituting (18) into (14), subtracting (15), and combining with (17), we can obtain the following:

$$\frac{\mathrm{d}\left(\mathbf{x_s} - \mathbf{x_{sref}}\right)}{\mathrm{d}t} = \mathbf{A_s}\left(\mathbf{x_s} - \mathbf{x_{sref}}\right)$$

$$+\mathbf{B_s}\left(\mathbf{C_{s2}B_s}\right)\left(-k_{s1}\mathbf{C_{s1}}\right)\left(\mathbf{x_s}-\mathbf{x_{sref}}\right)$$
$$+\mathbf{B_s}\left(\mathbf{C_{s2}B_s}\right)\left(-k_{s2}\mathbf{C_{s2}}-\mathbf{C_{s2}A_s}\right)\left(\mathbf{x_s}-\mathbf{x_{sref}}\right). \quad (19)$$

Equation (19) can be written in the following matrix form:

$$\frac{\mathrm{d}\left(\mathbf{x_s}-\mathbf{x_{sref}}\right)}{\mathrm{d}t}=\bar{\mathbf{A}}_\mathbf{s}\left(\mathbf{x_s}-\mathbf{x_{sref}}\right) \quad (20)$$

where

$$\bar{\mathbf{A}}_\mathbf{s}=\begin{bmatrix}0 & 1 & \cdots & 0\\ \vdots & \vdots & \cdots & \vdots\\ 0 & 0 & \cdots & 1\\ -\bar{k}_{s0} & -\bar{k}_{s1} & \cdots & -\bar{k}_{s(n-1)}\end{bmatrix}$$

$$\bar{k}_{s0}=\frac{c_{11}k_{s1}+c_{21}k_{s2}}{c_{2n}},$$

$$\bar{k}_{sj}=\frac{\left(c_{1(j+1)}k_{s1}+c_{2(j+1)}k_{s2}+c_{2j}\right)}{c_{2n}}\left(j=1,\ldots,n-1\right).$$

The characteristic polynomial of (20) is as follows:

$$f\left(\lambda\right)=\lambda^n+\bar{k}_{s(n-1)}\lambda^{n-1}+\cdots+\bar{k}_{s1}\lambda+\bar{k}_{s0}. \quad (21)$$

Write the coefficients of (21) in matrix form

$$\bar{\mathbf{K}}_\mathbf{s}=\frac{1}{C_{2n}}\mathbf{C_s^T}\mathbf{K_s}+\bar{\mathbf{B}}_\mathbf{s} \quad (22)$$

where

$$\bar{\mathbf{K}}_\mathbf{s}=\begin{bmatrix}\bar{k}_{s0}\\ \bar{k}_{s1}\\ \vdots\\ \bar{k}_{s(n-1)}\end{bmatrix},\ \mathbf{C_s^T}=\begin{bmatrix}c_{11} & c_{21}\\ c_{12} & c_{22}\\ \vdots & \vdots\\ c_{1n} & c_{2n}\end{bmatrix},\ \mathbf{K_s}=\begin{bmatrix}k_{s1}\\ k_{s2}\end{bmatrix},$$

$$\mathrm{B_s}=\begin{bmatrix}0\\ c_{21}/c_{2n}\\ \vdots\\ c_{2(n-1)}/c_{2n}\end{bmatrix}.$$

Select $\bar{k}_{sj}$in (21) by the pole-placement method. Then, by solving (22), the coefficients k_{s1} and k_{s2} of the control law (18) can be obtained. Equation (18) can be expressed as follows:

It can be known from (23) shown at the bottom of this page, that after obtaining k_{s1} and k_{s2}, the control coefficients k_1 and k_2 of the control law (12) are determined. It is worth noting that for system (4), once the output functions $h_1(x)=v_\mathrm{C}$ and $h_2(x)=i_\mathrm{L}$ are determined, no matter whether it is a linear or nonlinear load, the mathematical form of the control law (12) remains unchanged.

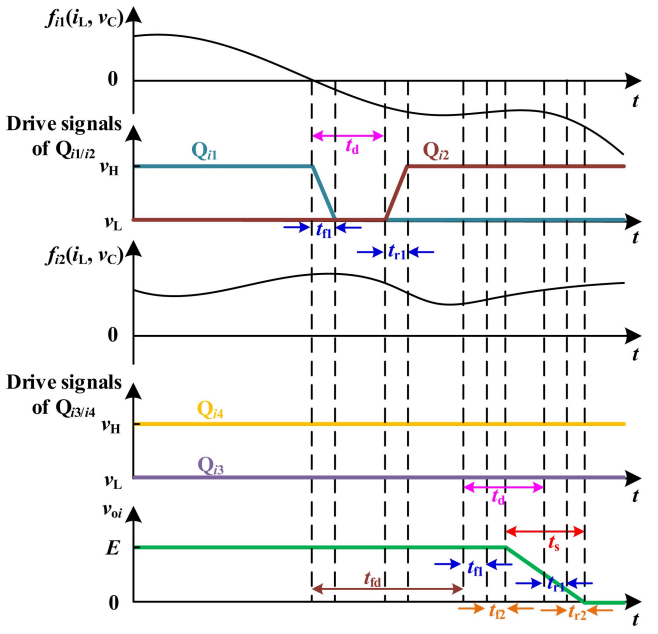

Fig. 3. Actual waveform schematic of v_{oi} switching from E to 0.

C. Determination of the Output Level

The continuous control law (12) cannot be used to directly determine the required switching-state combinations for controlling the switching devices. As shown in Table I, the switching-state combinations correspond to the output voltage level v_ab. Therefore, v_ab is determined first before identifying the switching-state combinations. According to (2)–(4), it follows that

$$u=\sum_{i=1}^{N}\left[S\left(af_{i1}\left(i_\mathrm{L},v_\mathrm{C}\right)\right)+S\left(af_{i2}\left(i_\mathrm{L},v_\mathrm{C}\right)\right)-N\right]\approx\psi. \quad (24)$$

The essence of (24) is to approximately describe the output voltage v_{oi} ($v_{oi}=(q_{i1}+q_{i2}-1)E$) of the ith unit by ($S(af_{i1}(i_\mathrm{L}, v_\mathrm{C}))+S(af_{i2}(i_\mathrm{L}, v_\mathrm{C}))-1)E$. In engineering applications, the waveform of v_{oi} is affected by factors such as switching delay time and dead-time, and it is a non-ideal rectangular wave. Therefore, by reasonably designing the value of the steepness factor a, the slope of the periodic sigmoid function curve can be adjusted to more accurately describe the actual waveform of v_{oi}. Taking v_{oi} switching from E to 0 as an example, Fig. 3 shows the switching schematic diagram of the actual waveform (assuming the controller is a DSP). t_{f1} is the DSP off-command

$$\begin{aligned}u_\mathrm{o}&=\left(\mathbf{C_{o2}B_s}\right)^{-1}\left[-k_{s1}\left(y_{s1}-y_{s1ref}\right)-k_{s2}\left(y_{s2}-y_{s2ref}\right)-\mathbf{C_{s2}A_sx_s}+\dot{y}_{s2ref}\right]\\&=\left(\mathbf{C_{o2}T_s^{-1}T_sB_o}\right)^{-1}\left[-k_{s1}\left(\mathbf{C_{s1}x_s}-\mathbf{C_{s1}x_{sref}}\right)-k_{s2}\left(\mathbf{C_{s2}x_s}-\mathbf{C_{s2}x_{sref}}\right)-\mathbf{C_{s2}A_sx_s}+\mathbf{C_{s2}A_sx_{sref}}+\mathbf{C_{s2}B_su_{oref}}\right]\\&=\left(\mathbf{C_{o2}T_s^{-1}T_sB_o}\right)^{-1}\left[-k_{s1}\left(\mathbf{C_{o1}T_s^{-1}T_sx_o}-\mathbf{C_{o1}T_s^{-1}T_sx_{oref}}\right)-k_{s2}\left(\mathbf{C_{o2}T_s^{-1}T_sx_o}-\mathbf{C_{o2}T_s^{-1}T_sx_{oref}}\right)\right.\\&\quad\left.-\mathbf{C_{o2}T_s^{-1}A_sT_sx_o}\right]\\&\quad+\left(\mathbf{C_{o2}T_s^{-1}T_sB_o}\right)^{-1}\left(\mathbf{C_{o2}T_s^{-1}A_sT_sx_{oref}}+\mathbf{C_{o2}T_s^{-1}T_sB_o}u_{oref}\right)\\&=\left(\mathbf{C_{o2}B_o}\right)^{-1}\left[-k_{s1}\left(y_{o1}-y_{o1ref}\right)-k_{s2}\left(y_{o2}-y_{o2ref}\right)-\mathbf{C_{o2}A_ox_o}+\dot{y}_{o2ref}\right].\end{aligned} \quad (23)$$

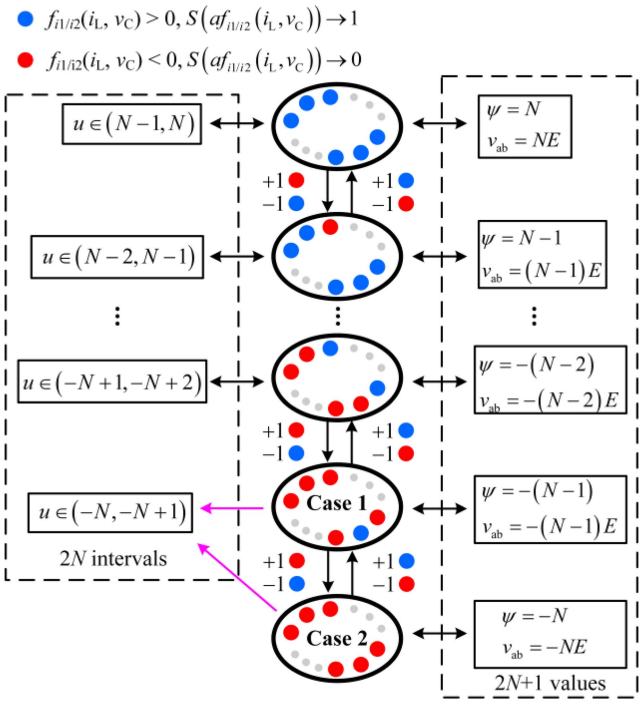

Fig. 4. Schematic diagram of establishing the corresponding relationship among u, ψ, and v_{ab} based on the sigmoid function.

delay time, t_d is the dead-time, t_{r1} is the DSP on-command delay time, t_{f2} is the switch-off delay time, t_{r2} is the switch-on delay time, and t_{fd} is the drive signal transmission delay time. t_{f1}, t_{r1}, t_{f2}, t_{r2}, and t_{fd} can all be obtained by referring to the datasheets of the DSP, switches, and driver chips. As shown in Fig. 3, the time t_s for v_{oi} to switch from E to 0 is $t_s = t_d - t_{f1} - t_{f2} + t_{r1} + t_{r2}$, and the absolute value of its slope is E/t_s. When $f_{i2}(i_L, v_C)$ remains greater than zero, it is approximately considered that the value of $S(af_{i2}(i_L, v_C)) - 1$ approaches 0, and the waveform of v_{oi} is described by $S(af_{i1}(i_L, v_C))E$. When the value of f_{i1} (i_L, v_C) changes from positive to negative, at $f_{i1}(i_L, v_C) = 0$, the maximum absolute value of the slope of $S(f_{i1}(i_L, v_C))E$ is $0.25aE$. Therefore, to better fit the actual waveform of v_{oi} switching from E to 0, let $0.25aE = E/t_s$. Then the selection of the steepness factor a should satisfy

$$a = 4/t_s. \tag{25}$$

As the sigmoid function has the value domain (0, 1), u is bounded and has the value domain ($-N$, N). ψ takes values in the discrete set $\{-N, (-N+1), (-N+2), \ldots, N-1, N\}$. And, since a is large enough, the value of the sigmoid function can be approximated as 0 or 1. Therefore, as shown in Fig. 4, the domain of values of u can be divided into $2N$ intervals of length 1. After the discrete variables q_{i1} and q_{i2} are approximately replaced by $S(af_{i1}(i_L, v_C))$ and $S(af_{i2}(i_L, v_C))$, respectively, ψ has $2N+1$ kinds of values. There is a problem that the value-taking interval of u and the value of ψ cannot be in one-to-one correspondence. The reason is that the following two situations will both lead to u being in the same value-taking interval $(-N, -N+1)$ (as shown by the pink arrow in Fig. 4):

TABLE III
CORRESPONDING RELATIONSHIPS AMONG u, ψ, AND v_{AB}

Interval of u	ψ	v_{ab}
$(N-1, N)$	N	NE
$(N-2, N-1)$	$N-1$	$(N-1)E$
⋮	⋮	⋮
$(-N+1, -N+2)$	$-(N-2)$	$-(N-2)E$
$(-N+\delta, -N+1)$	$-(N-1)$	$-(N-1)E$
$(-N, -N+\delta)$	$-N$	$-NE$

Case 1: When there is only one f_{i1} (i_L, v_C) greater than 0 or only one f_{i2} (i_L, v_C) greater than 0, $u \in (-N, -N+1)$.

Case 2: When all $f_{11/12}(i_L, v_C) - f_{N1/N2}(i_L, v_C)$ are less than 0, u is also in $(-N, -N+1)$.

Therefore, it is important to distinguish between the two situations. Assuming $u \in (-N+\delta, -N+1)$ when Case 1 occurs and $u \in (-N, -N+\delta)$ when Case 2 occurs. Combining with (2) and (24), the correspondence between u, ψ, and v_{ab} can be obtained as shown in Table III.

According to Table III, without loss of generality, assume that the function values of $f_{11}(i_L, v_C) - f_{N1}(i_L, v_C)$ and $f_{12}(i_L, v_C) - f_{N2}(i_L, v_C)$ are always randomly assigned without replacement from the set Φ: $\{u-(N-1), u-(N-2), \cdots, u-(-N+1), u-(-N+\delta)\}$. Therefore, when Case 1 occurs $(u \in (-N+\delta, -N+1))$, it can be obtained based on (24)

$$\begin{aligned} &S(a(u-(N-1))) + S(a(u-(N-2))) + \cdots \\ &\quad + S(a(u-(-N+1))) + S(a(u-(-N+\delta))) > \delta. \end{aligned} \tag{26}$$

Since the sigmoid function is a monotonically increasing function. When $u = -N+\delta$, there is

$$\begin{aligned} &S(a(\delta-2N+1)) + S(a(\delta-2N+2)) + \cdots \\ &\quad + S(a(\delta-1)) + 0.5 \geq \delta. \end{aligned} \tag{27}$$

When Case 2 occurs, $u \in (-N, -N+\delta)$, it can be obtained based on (24)

$$\begin{aligned} &S(a(u-(N-1))) + S(a(u-(N-2))) + \cdots \\ &+ S(a(u-(-N+1))) + S(a(u-(-N+\delta))) < \delta. \end{aligned} \tag{28}$$

When $u = -N+\delta$, there is

$$\begin{aligned} &S(a(\delta-2N+1)) + S(a(\delta-2N+2)) + \cdots \\ &\quad + S(a(\delta-1)) + 0.5 \leq \delta. \end{aligned} \tag{29}$$

If (27) and (29) need to be satisfied simultaneously, then there is

$$\delta = 0.5 + \Delta \tag{30}$$

where

$$\begin{aligned} \Delta = &S(a(\delta-2N+1)) + S(a(\delta-2N+2)) \\ &+ \cdots + S(a(\delta-1)). \end{aligned} \tag{31}$$

Equation (30) is a transcendental equation, and it is difficult to obtain the analytical solution of δ. The Newton-Raphson iterative method is used to solve δ. Based on (25), select $a = 1 \times 10^6$. Let $f(\delta) = 0.5 + S(a(\delta-2N+1)) + S(a(\delta-2N+2)) + \cdots + S(a(\delta-1))$, then the iterative equation is $\delta_{n+1} = f(\delta_n)$. Under different initial value conditions, it is found that δ converges

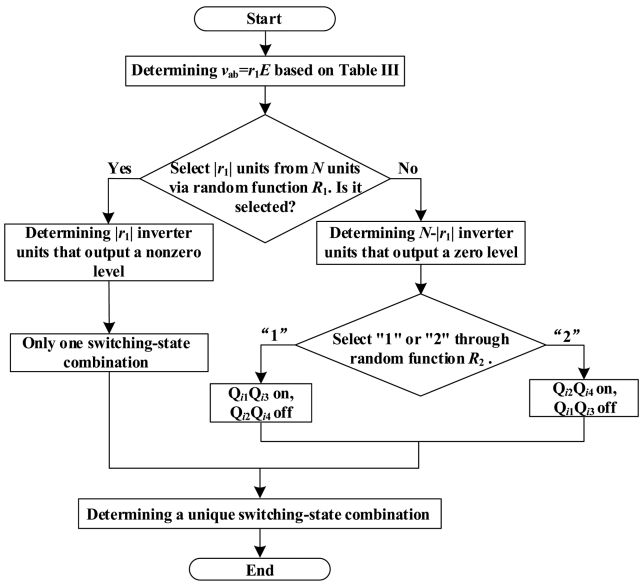

Fig. 5. Flowchart of determining a unique switching-state combination by two random selections for symmetric CHBMI.

to 0.5 and is independent of N, so Δ can be neglected. After obtaining the value of δ, the output level v_{ab} of the symmetric CHBMI can be determined according to the control law (12) and Table III.

D. Two Random Selections and Mechanism of Power Balancing

However, even after determining v_{ab}, Table I shows that a unique switching-state combination can be identified only when v_{ab} takes the values *NE* and *–NE*. When v_{ab} takes other values, it corresponds to multiple different combinations. To address this, use two random selections to determine a unique combination while achieving power balancing of all the inverter units. The implementation steps are shown in Fig. 5, and the specific process is as follows: first, $v_{\mathrm{ab}} = r_1E$ ($r_1 = -N, \ldots, 0, \ldots, N$) is determined according to Table III after obtaining the control law u based on (12). Here, $|r_1|$ inverter units need to generate E or $-E$. Subsequently, a random function R_1 is used to select $|r_1|$ units among N inverter units randomly. Depending on the output of R_1, the inverter unit that provides a nonzero level or the inverter unit that provides a zero level can be selected. There is only one switching-state combination for inverter units with a nonzero output level. For units with a zero level, there are two possible combinations ("1" and "2," as described in Section II), and one of them is selected using the random function R_2. Thus, a unique switching-state combination can be determined through the two random selections. The mechanism for achieving power balancing is also revealed as follows.

According to the law of large numbers in probability theory, if the inverter unit has an equal probability of being selected by R_1 to provide a nonzero level (including E and $-E$), then the time each unit spends producing nonzero levels will converge to the same value over a sufficiently long period. From the point of view of statistical average significance, we can assume that the time intervals corresponding to the output levels E, 0, and $-E$ of each inverter unit in a fundamental wave period T are t_1, t_2, and $T - t_1 - t_2$, respectively. Assuming that the output voltage $v_{\mathrm{o}i}(t)$ of any ith inverter unit within the nth ($n \geq 1$) period T is represented as

$$v_{oi}(t) = \begin{cases} E, & (n-1)T \leq t < (n-1)T + t_1 \\ 0, & (n-1)T + t_1 \leq t < (n-1)T + t_1 + t_2 \\ -E, & (n-1)T + t_1 + t_2 \leq t < nT \end{cases}. \tag{32}$$

Expanding it into a Fourier series

$$v_{oi}(t) = a_{i0} + \sum_{n=1}^{\infty} \left(a_{in}\cos(n\omega t) + b_{in}\sin(n\omega t)\right) \tag{33}$$

where a_{i0} is the dc component, a_{in} and b_{in} are the coefficients of the sine and cosine terms of each harmonic, respectively, and $\omega = 2\pi/T$. The coefficients a_{i1} and b_{i1} of the fundamental wave component $v_{\mathrm{o}i1}(t)$ are, respectively

$$\begin{aligned} a_{i1} &= \frac{2}{T}\int_{(n-1)T}^{nT} v_{oi}(t)\cos(\omega t)\,\mathrm{d}t \\ &= \frac{2}{T}E\frac{\sin(\omega t_1)}{\omega} + \frac{2}{T}E\frac{\sin(\omega(t_1+t_2))}{\omega} \end{aligned} \tag{34}$$

$$\begin{aligned} b_{i1} &= \frac{2}{T}\int_{(n-1)T}^{nT} v_{oi}(t)\sin(\omega t)\,\mathrm{d}t \\ &= \frac{2}{T}\left(-E\frac{\cos(\omega t_1)-1}{\omega}\right) + \frac{2}{T}\left(E\frac{1-\cos(\omega(t_1+t_2))}{\omega}\right). \end{aligned} \tag{35}$$

As t_1 and t_2 are the same for all inverter units, their fundamental wave components are equal.

When the CHBMI operates stably, $i_{\mathrm{L}}(t)$ approximates a sine wave and is approximately equal to its fundamental waveform component: $i_{\mathrm{L}}(t) \approx i_{\mathrm{L}1}(t) = c_1\cos(\omega t) + d_1\sin(\omega t)$, where c_1 and d_1 are constants. The average output power P_i of the ith inverter unit in one period T is

$$P_i \approx \frac{\int_{(n-1)T}^{nT}\left(a_{i0} + \sum_{n=1}^{\infty}\left(a_{in}\cos(n\omega t) + b_{in}\sin(n\omega t)\right)\right) i_{\mathrm{L}1}(t)\,\mathrm{d}t}{T}. \tag{36}$$

Using trigonometric product formulas and orthogonality, this can also be expressed as follows:

$$P_i \approx \frac{V_{oi1\mathrm{m}}I_{\mathrm{L}1\mathrm{m}}}{2}\cos\theta = \frac{\sqrt{{a_{i1}}^2 + {b_{i1}}^2}\sqrt{{c_1}^2 + {d_1}^2}}{2}\cos\theta \tag{37}$$

where $V_{oi1\mathrm{m}}$ is the amplitude of $v_{\mathrm{o}i1}(t)$, $I_{\mathrm{L}1\mathrm{m}}$ is the amplitude of $i_{\mathrm{L}1}(t)$, and θ is the phase difference between $v_{\mathrm{o}i1}(t)$ and $i_{\mathrm{L}1}(t)$. From (37), whether the average power balancing of the output of each inverter unit can be realized mainly depends on whether the fundamental wave components of the output voltage of each inverter unit are equal. From the previous analysis, by performing two random selections, the fundamental voltage components can be ensured to be equal for all inverter units, thus achieving power balancing.

Fig. 6 illustrates the control block diagram of the proposed method. As shown in Fig. 6, the proposed method directly controls the switching devices based on the control law u and

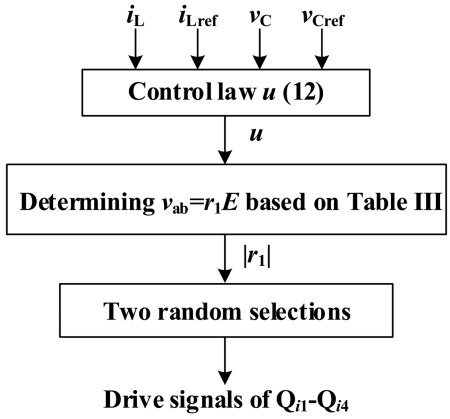

Fig. 6. Control block diagram of the proposed method.

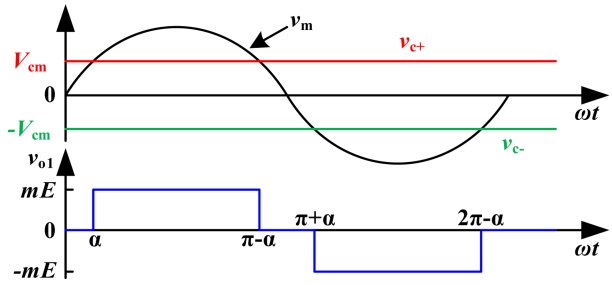

Fig. 7. Staircase modulation of high-voltage inverter unit 1.

two random selections, eliminating the need to simultaneously generate multiple different carrier signals or evaluate switching-state combinations. This is beneficial to reduce the control cost (without the need to use expensive FPGA) or reduce the execution time. Consequently, the proposed method maintains good applicability even as the number of inverter units N increases.

IV. Extension of the Proposed Control Method to Asymmetric CHBMI

The proposed control method is extended to the asymmetric CHBMI (see Fig. 1, where $m > 1$). To reduce the loss of switching devices, it is expected that the high-voltage unit 1 operates in a low-frequency state. Therefore, the staircase modulation shown in Fig. 7 is adopted for unit 1 to make it operate in the fundamental frequency state. The given modulation wave signal is $v_m = V_m \sin\omega t$. v_{c+} and v_{c-} are carrier signals, and their amplitudes are V_{cm} and $-V_{cm}$, respectively. The specific switching control logic is: when $v_m > v_{c+}$, $q_{11} = 1$, $q_{12} = 1$, $v_{o1} = mE$; when $v_m < v_{c+}$ and $v_m > v_{c-}$, $q_{11} = 0$, $q_{12} = 1$, $v_{o1} = 0$; when $v_m < v_{c-}$, $q_{11} = 0$, $q_{12} = 0$, $v_{o1} = -mE$. The switching control logic can be described by the step function:

$$q_{11/12} = H\left(v_m - v_{c+/c-}\right) = \begin{cases} 1, & v_m - v_{c+/c-} > 0 \\ 0, & v_m - v_{c+/c-} < 0 \end{cases}. \quad (38)$$

Fix $V_m = 1$, then the conduction angle α in Fig. 7 is determined by the carrier amplitude V_{cm}

$$\alpha = \arcsin\left(V_{cm}\right). \quad (39)$$

The Fourier series expansion of the output voltage v_{o1} of the high-voltage unit 1 is

$$v_{o1} = \frac{4mE}{\pi} \sum_{k=1,3,5,\cdots}^{\infty} \frac{1}{k} \cos\left(k\alpha\right) \sin\left(k\omega t\right). \quad (40)$$

The amplitude V_{o11m} of the fundamental wave voltage of its output voltage can be expressed as follows:

$$V_{o11m} = \frac{4mE}{\pi} \cos\alpha. \quad (41)$$

To achieve the balance of output power between the high- and low-voltage units, the output power of the high-voltage unit 1 should be m times that of the low-voltage units 2−N. That is, the amplitude of the fundamental wave voltage of v_{o1} should be m times that of v_{o2}−v_{oN}. Suppose the reference voltage of the asymmetric CHBMI is $v_{Cref} = V_{Crefm} \sin(\omega t)$, then V_{o11m} needs to satisfy

$$V_{o11m} = \frac{m}{N - 1 + m} V_{Crefm}. \quad (42)$$

Based on (39), (41), and (42), the expression of the carrier amplitude V_{cm} can be obtained

$$V_{cm} = \sin\left(\arccos\left(\frac{V_{Crefm}\pi}{4E\left(N - 1 + m\right)}\right)\right). \quad (43)$$

On the basis of using staircase-wave modulation for the high-voltage unit, the proposed method is adopted. Assume that the discrete switching variables q_{21}−q_{N1} and q_{22}−q_{N2} of the low-voltage units 2−N are determined by the continuous functions $f_{21}(i_L, v_C)$−$f_{N1}(i_L, v_C)$ and $f_{22}(i_L, v_C)$−$f_{N2}(i_L, v_C)$. The specific control logic is: when $f_{j1}(i_L, v_C) > 0$, $q_{j1} = 1$; when $f_{j1}(i_L, v_C) < 0$, $q_{j1} = 0$; when $f_{j2}(i_L, v_C) > 0$, $q_{j2} = 1$; when $f_{j2}(i_L, v_C) < 0$, $q_{j2} = 0$ ($j = 2, 3, \ldots, N$). Thus, the relationship between $f_{j1/j2}(i_L, v_C)$ and $q_{j1/j2}$ can also be described using the step function

$$q_{j1/j2} = H\left(f_{j1/j2}\left(i_L, v_C\right)\right) = \begin{cases} 1, & f_{j1/j2}\left(i_L, v_C\right) > 0 \\ 0, & f_{j1/j2}\left(i_L, v_C\right) < 0 \end{cases}. \quad (44)$$

Based on (38) and (44), the output level v_{ab} of the asymmetric CHBMI can be expressed by the sigmoid function as

$$v_{ab} \approx \left(\left(S\left(a\left(v_m - v_{c+}\right)\right) + S\left(a\left(v_m - v_{c-}\right)\right)\right) - 1\right) mE + \left(\sum_{j=2}^{N} \left(S\left(af_{j1}\left(i_L, v_C\right)\right) + S\left(af_{j2}\left(i_L, v_C\right)\right)\right) - (N - 1)\right) E. \quad (45)$$

It is worth noting that when modeling the symmetric CHBMI and the asymmetric CHBMI based on the sigmoid function, the difference between the two is only that the expressions of v_{ab} are different [i.e., (3) and (45) are different]. Therefore, the asymmetric CHBMI can also obtain a continuous and smooth sigmoid function model consistent with the form of (4). Using the method introduced in Section III-B, the control law u of the asymmetric CHBMI consistent with the form of (12) can be obtained, which will not be repeated here.

Since the high-voltage unit 1 has adopted staircase modulation, only the control of the low-voltage units 2−N needs to be considered. Based on (4), (12), and (45), the control law u_L of the low-voltage units 2−N is obtained

$$u_L = u - m\left(\left(S\left(a\left(v_m - v_{c+}\right)\right) + S\left(a\left(v_m - v_{c-}\right)\right)\right) - 1\right)$$

TABLE IV
CORRESPONDING RELATIONSHIPS AMONG u_{L}, ψ_{L}, AND v_{oL}

Interval of u_{L}	ψ_{L}	v_{oL}
$(N\text{–}2, N\text{–}1)$	$N\text{–}1$	$(N\text{–}1)E$
$(N\text{–}3, N\text{–}2)$	$N\text{–}2$	$(N\text{–}2)E$
⋮	⋮	⋮
$(-N\text{+}2, -N\text{+}3)$	$-(N\text{–}3)$	$-(N\text{–}3)E$
$(-(N\text{–}1)\text{+}0.5, -N\text{+}2)$	$-(N\text{–}2)$	$-(N\text{–}2)E$
$(-(N\text{–}1), -(N\text{–}1)\text{+}0.5)$	$-(N\text{–}1)$	$-(N\text{–}1)E$

$$= \frac{-k_1 I_1 - k_2 I_2 - L_f h_2(x) + \dot{y}_{2\mathrm{ref}}}{L_g L_f^0 h_2(x)}$$

$$-m\left(\left(S\left(a\left(v_{\mathrm{m}} - v_{\mathrm{c}+}\right)\right) + S\left(a\left(v_{\mathrm{m}} - v_{\mathrm{c}-}\right)\right)\right) - 1\right). \quad (46)$$

Based on (2), (38), and (46), we can obtain the following:

$$u_{\mathrm{L}} \approx \psi - m\left(q_{11} + q_{12} - 1\right) = \sum_{j=2}^{N} \left(q_{j1} + q_{j2} - (N-1)\right). \quad (47)$$

Let $\psi_{\mathrm{L}} = \sum_{j=2}^{N}\left(q_{j1} + q_{j2} - (N-1)\right)$. Use $v_{\mathrm{oL}} = v_{\mathrm{o}2} + v_{\mathrm{o}3} + \ldots + v_{\mathrm{o}N}$ to represent the total output level of the low-voltage units. Using the method introduced in Section III-C, a one-to-one correspondence relationship among u_{L}, ψ_{L}, and v_{oL} is established by the sigmoid function, as shown in Table IV.

Therefore, after obtaining the control law (46) of low-voltage units, the total output level v_{oL} of low-voltage units can be determined according to Table IV. Through two random selections, the unique switching-state combination of low-voltage units of the asymmetric CHBMI can be obtained.

The main difference between applying the proposed method to the symmetric CHBMI and the asymmetric CHBMI is as follows: After obtaining the control law (12) based on the sigmoid function model (4), for the symmetric CHBMI, what needs to be determined is the total level v_{ab} of the sum of the output voltages of all inverter units, and then the switching-state combination of all units is determined by two random selections; while for the asymmetric CHBMI, due to the combination of the staircase modulation of the high-voltage unit, it is necessary to separate the control law u_{L} of the low-voltage unit from the control law (12), and then determine the sum v_{oL} of the output levels of all low-voltage units. Finally, the switching-state combination of all low-voltage units is determined by two random selections.

V. SIMULATION VALIDATION

To verify the effectiveness and superiority of the proposed method, simulations were conducted on the MATLAB/Simulink platform for both a symmetric CHBMI ($m = 1$) with 1:1:1 dc-side voltage ratio and an asymmetric CHBMI ($m = 2$) with 2:1:1 dc-side voltage ratio. The symmetric CHBMI was connected to a linear resistive load R_{L} as shown in Fig. 8(a), while the asymmetric CHBMI drove a nonlinear rectifier load illustrated in Fig. 8(b). The system performance was evaluated through three aspects: steady-state performance, dynamic performance, and power balancing capability.

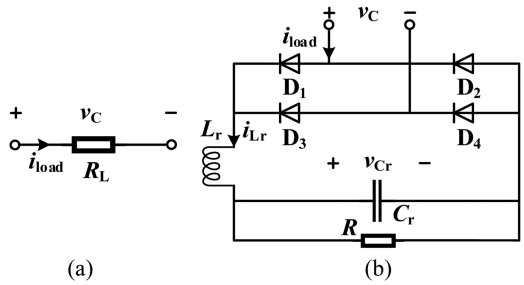

Fig. 8. Loads. (a) Linear resistive load. (b) Nonlinear rectifier load.

TABLE V
MAIN SIMULATION PARAMETERS OF SYMMETRIC CHBMI

Symbol	Parameters	Values
E	DC source voltage	200 V
V_{Crefin}	Amplitude of the reference voltage v_{Cref}	500/530 V
T	Period of the reference voltage v_{Cref}	0.02 s
L	Filter inductor	1 mH
C	Filter capacitor	10 μF
R_{L}	Resistive load	30 Ω

In this section, part A presents the simulation results when the proposed method, PS-PWM-based PI control [10], CR-LS-PWM-based PI control [13], and improved FCS-MPC [23] are respectively applied to the symmetric CHBMI; part B presents the simulation results when the proposed method, PBIH-PWM-based PI control [14], and improved FCS-MPC [23] are respectively applied to the asymmetric CHBMI.

A. Simulation Results of Symmetric CHBMI

The simulation parameter settings are shown in Table V. The sigmoid function model of the symmetric CHBMI is

$$\begin{cases} \dot{x}_1 = \frac{\mathrm{d}i_{\mathrm{L}}}{\mathrm{d}t} = -\frac{v_{\mathrm{C}}}{L} + \frac{E}{L}u \\ \dot{x}_2 = \frac{\mathrm{d}v_{\mathrm{C}}}{\mathrm{d}t} = \frac{i_{\mathrm{L}}}{C} - \frac{v_{\mathrm{C}}}{R_{\mathrm{L}}C} \\ y_1 = v_{\mathrm{C}}, y_2 = i_{\mathrm{L}} \end{cases}. \quad (48)$$

According to Section III-B, the control coefficients of the proposed method were designed as $k_1 = 58\,900$ and $k_2 = 125\,000$. A dual-loop structure was employed in PS-PWM-based PI control and CR-LS-PWM-based PI control. Considering the impact of PI control coefficients on stability and dynamic response [29], the voltage loop PI coefficients were set as $k_{\mathrm{pv}} = 5$ and $k_{\mathrm{iv}} = 200$, while the current loop PI coefficients were set as $k_{\mathrm{pc}} = 0.5$ and $k_{\mathrm{ic}} = 5$. The improved FCS-MPC takes v_{ab} as the optimization variable instead of the switching-state combination to reduce the calculation burden. Its discrete prediction model is

$$\begin{cases} i_{\mathrm{L}j}(k+1) = \left[\frac{-v_{\mathrm{C}}(k)}{L} + \frac{v_{\mathrm{ab}j}}{L}\right] T_{\mathrm{s}} + i_{\mathrm{L}}(k) \\ v_{\mathrm{C}j}(k+1) = \left[\frac{i_{\mathrm{L}j}(k+1)}{C} - i_{\mathrm{load}}(k)\right] T_{\mathrm{s}} + v_{\mathrm{C}}(k) \end{cases} \quad (49)$$

where T_{s} denotes the sampling period, $j = 1, 2, \ldots, 2N+1$. $i_{\mathrm{L}}(k)$, $v_{\mathrm{C}}(k)$, and $i_{\mathrm{load}}(k)$ respectively represent the sampled inductor current, output voltage, and load current in the kth period. $v_{\mathrm{ab}j}$ represents the jth output level. $i_{\mathrm{L}j}(k+1)$ and $v_{\mathrm{C}j}(k+1)$ respectively denote the predicted current and voltage at the

TABLE VI
STEADY-STATE AND DYNAMIC PERFORMANCE INDICATORS OF SYMMETRIC CHBMI UNDER DIFFERENT CONTROL METHODS

	Proposed control method	PS-PWM-based PI control [10]	CR-LS-PWM-based PI control [13]	Improved FCS-MPC [23]
THD of v_{ab} (V_{Crefm} = 500/530 V)	23.90%/22.64%	34.93%/32.18%	24.92%/23.65%	24.52%/23.78%
THD of v_C (V_{Crefm} = 500/530 V)	0.23%/0.23%	0.43%/0.31%	0.41%/0.34%	0.31%/0.27%
RMSE of v_C (V_{Crefm} = 500/530 V)	0.1388/0.1392 V	2.5177/2.6417 V	3.0685/3.2572 V	0.1432/0.1451 V
RMSE of i_L (V_{Crefm} = 500/530 V)	0.0457/0.0486 A	0.2289/0.2265 A	0.2268/0.2285 A	0.0503/0.0501 A
v_{ab} and v_{o1}–v_{o3} have level jumps?	No	Yes	Yes	No
Maximum fluctuation of v_C/i_L	0 V/4.8 A	11.5 V/9.9 A	11.1 V/9.7 A	0 V/3.4 A
Dynamic response time	0.12 ms	0.31 ms	0.41 ms	0.18 ms
Power balance degree	99.57%	98.94%	98.89%	–32.73%

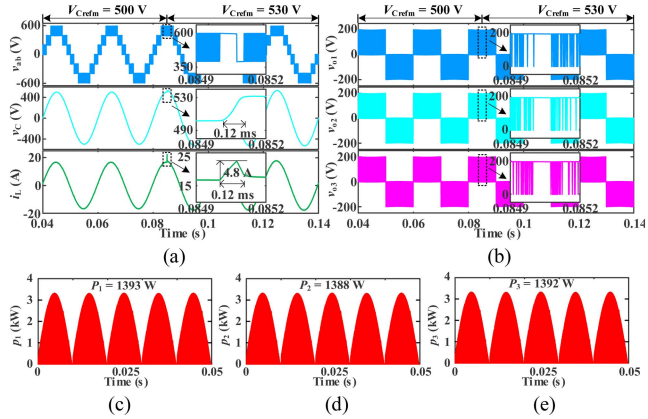

Fig. 9. Simulation results of symmetric CHBMI under the proposed control method. (a) Waveforms of v_{ab}, v_C, and i_L. (b) Waveforms of v_{o1}, v_{o2}, v_{o3}. Instantaneous power and average power when $V_{Crefm} = 500$ V: (c) p_1 and P_1; (d) p_2 and P_2; and (e) p_3 and P_3.

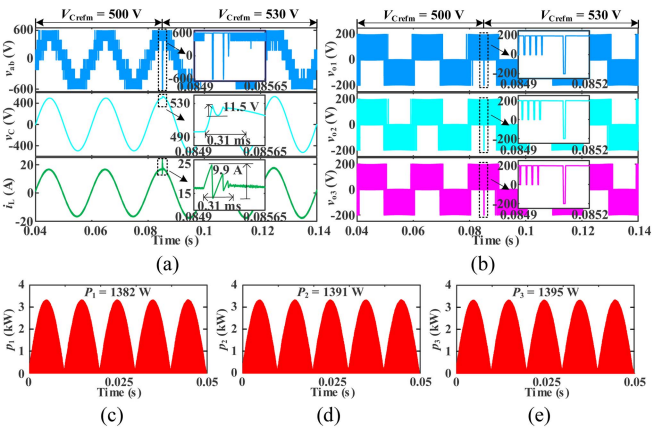

Fig. 10. Simulation results of symmetric CHBMI under PS-PWM-based PI control. (a) Waveforms of v_{ab}, v_C, and i_L. (b) Waveforms of v_{o1}, v_{o2}, v_{o3}. Instantaneous power and average power when $V_{Crefm} = 500$ V: (c) p_1 and P_1; (d) p_2 and P_2; and (e) p_3 and P_3.

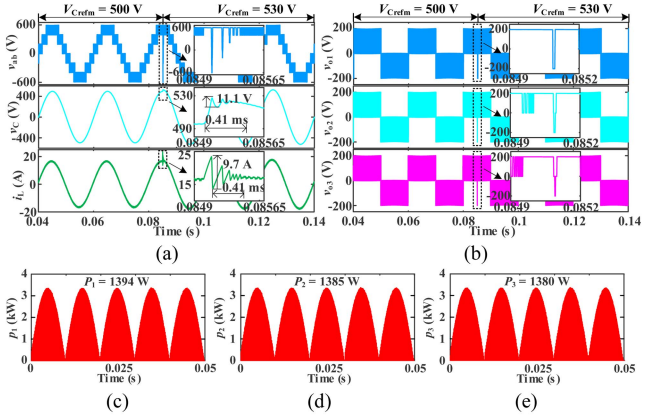

Fig. 11. Simulation results of symmetric CHBMI under CR-LS-PWM-based PI control. (a) Waveforms of v_{ab}, v_C, and i_L. (b) Waveforms of v_{o1}, v_{o2}, v_{o3}. Instantaneous power and average power when $V_{Crefm} = 500$ V: (c) p_1 and P_1; (d) p_2 and P_2; and (e) p_3 and P_3.

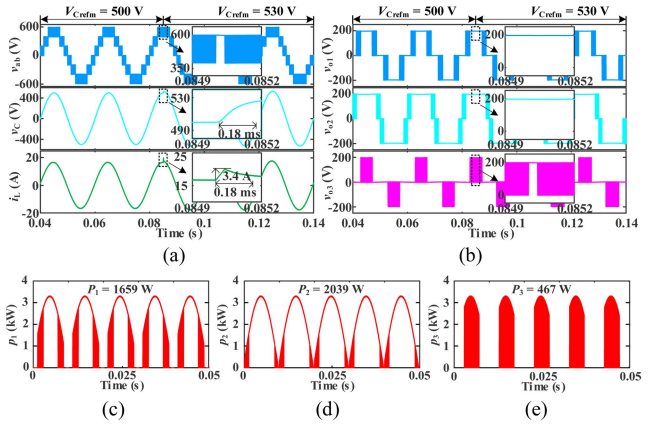

Fig. 12. Simulation results of symmetric CHBMI under improved FCS-MPC. (a) Waveforms of v_{ab}, v_C, and i_L. (b) Waveforms of v_{o1}, v_{o2}, v_{o3}. Instantaneous power and average power when $V_{Crefm} = 500$ V: (c) p_1 and P_1; (d) p_2 and P_2; and (e) p_3 and P_3.

$(k+1)$th period of the jth output level. The cost function is

$$G = G_1[i_{Lref}(k+1) - i_{Lj}(k+1)]^2 + G_2\left[v_{Cref}(k+1) - v_{Cj}(k+1)\right]^2 \quad (50)$$

where G_1 and G_2 are weighting factors. Since the tracking control of voltage and current is equally important, let $G_1 = G_2 = 1$. $i_{Lref}(k+1)$ and $v_{Cref}(k+1)$ denote the reference current and voltage at period $k+1$, respectively. Figs. 9–12 show the simulation results of the proposed method, PS-PWM-based PI control, CR-LS-PWM-based PI control, and improved FCS-MPC. When $t = 0.085$ s, the value of V_{Crefm} increased from 500 to 530 V. Table VI gives the steady-state and dynamic performance indicators, such as the THD of v_{ab} and v_C, the root mean square error (RMSE) of v_C and i_L, the maximum fluctuation values of v_C and i_L after the mutation of V_{Crefm}, the dynamic response

TABLE VII
MAIN SIMULATION PARAMETERS OF ASYMMETRIC CHBMI

Symbol	Parameters	Values
mE, E	DC-side voltage of unit 1, units 2–3	300 V, 150 V
V_{Crefm}	Amplitude of reference voltage v_{Cref}	500/530 V
T	Period of reference voltage v_{Cref}	0.02 s
L, L_{r}	Filter inductor	1 mH, 0.2 mH
C, C_{r}	Filter capacitor	1 μF
R	Resistive load	20 Ω

time, and the output power balance degree when different control methods are applied to the symmetric CHBMI. As shown in Table VI, when $V_{\mathrm{Crefm}} = 500/530$ V with the proposed method applied, the THD of v_{ab} is 23.90%/22.64%, the THD of v_{C} is 0.23%/0.23%, the RMSE of v_{C} is 0.1388/0.1392 V, and the RMSE of i_{L} is 0.0457/0.0486 A. These results indicate that the proposed method achieves the lowest THD and RMSE for the symmetric CHBMI compared to other methods. In addition, when V_{Crefm} mutates, there is no level jump in v_{ab} and $v_{\mathrm{o1}}-v_{\mathrm{o3}}$ of the symmetric CHBMI when the proposed method is applied, while both PS-PWM-based PI control and CR-LS-PWM-based PI control have jumps. Although the maximum fluctuation value of i_{L} of the proposed method is slightly higher than that of the improved FCS-MPC, the dynamic response time of v_{C} and i_{L} is the shortest, only 0.12 ms. In terms of power balance, the power balance degree of the proposed method is as high as 99.57%, which is significantly better than −32.73% of the improved FCS-MPC.

Therefore, according to the analysis of simulation results, for symmetric CHBMI, compared with the other three methods, the proposed method has comprehensive advantages in steady-state accuracy, dynamic response speed, and power balance.

B. Simulation Results of Asymmetric CHBMI

The simulation parameter settings are shown in Table VII. The sigmoid function model of the asymmetric CHBMI with a nonlinear rectifier load is

$$\begin{cases} \dot{x}_1 = \frac{\mathrm{d}i_{\mathrm{L}}}{\mathrm{d}t} = -\frac{v_{\mathrm{C}}}{L} + \frac{E}{L}u \\ \dot{x}_2 = \frac{\mathrm{d}v_{\mathrm{C}}}{\mathrm{d}t} = \frac{i_{\mathrm{L}}}{C} - \frac{i_{\mathrm{Lr}}(2S(av_{\mathrm{C}})-1)}{C} \\ \dot{x}_3 = \frac{\mathrm{d}i_{\mathrm{Lr}}}{\mathrm{d}t} = \frac{v_{\mathrm{C}}(2S(av_{\mathrm{C}})-1)}{L_{\mathrm{r}}} - \frac{v_{\mathrm{Cr}}}{L_{\mathrm{r}}} \\ \dot{x}_4 = \frac{\mathrm{d}v_{\mathrm{Cr}}}{\mathrm{d}t} = \frac{i_{\mathrm{Lr}}}{C_{\mathrm{r}}} - \frac{v_{\mathrm{Cr}}}{C_{\mathrm{r}}R} \\ y_1 = v_{\mathrm{C}},\ y_2 = i_{\mathrm{L}} \end{cases} . \tag{51}$$

According to Section III-B, the control coefficients of the proposed method were designed as $k_1 = 353\,000$, $k_2 = 112\,800$. Considering the impact of PI control coefficients on stability and dynamic response [29], the control coefficients of PBIH-PWM-based PI control were designed as: $k_{\mathrm{pv}} = 8$, $k_{\mathrm{iv}} = 300$, $k_{\mathrm{pc}} = 1.5$, $k_{\mathrm{ic}} = 280$. The discrete prediction model and cost function of the improved FCS-MPC are still (49) and (50). Figs. 13–15 respectively show the simulation results of using the proposed method, PBIH-PWM-based PI control [14], and the improved FCS-MPC [23]. When $t = 0.085$ s, the value of V_{Crefm} increased from 500 V to 530 V. Table VIII gives the steady-state and dynamic performance indicators when different

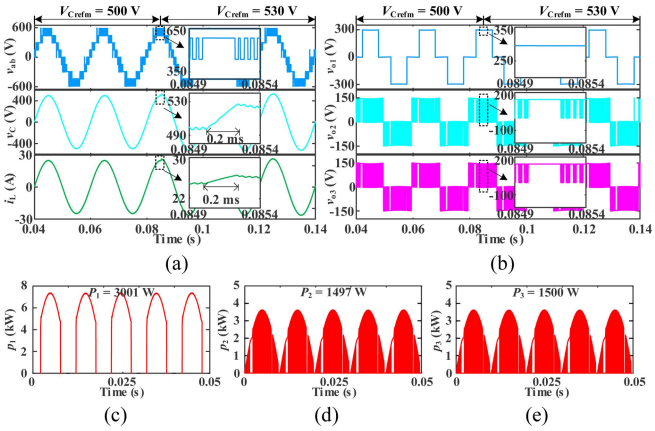

Fig. 13. Simulation results of asymmetric CHBMI under the proposed control method. (a) Waveforms of v_{ab}, v_{C}, and i_{L}. (b) Waveforms of v_{o1}, v_{o2}, v_{o3}. Instantaneous power and average power when $V_{\mathrm{Crefm}} = 500$ V: (c) p_1 and P_1; (d) p_2 and P_2; and (e) p_3 and P_3.

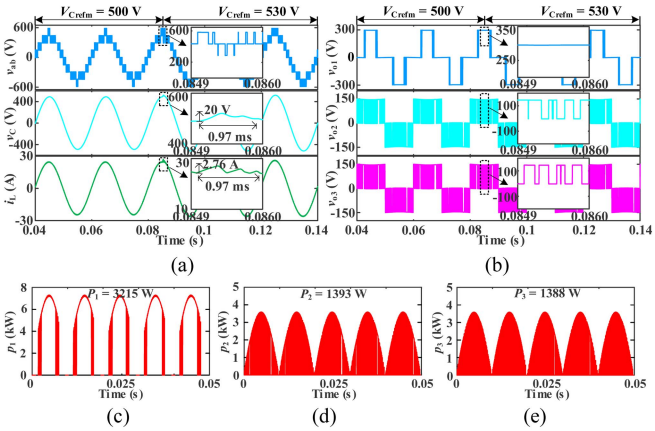

Fig. 14. Simulation results of asymmetric CHBMI under PBIH-PWM-based PI control. (a) Waveforms of v_{ab}, v_{C}, and i_{L}. (b) Waveforms of v_{o1}, v_{o2}, v_{o3}. Instantaneous power and average power when $V_{\mathrm{Crefm}} = 500$ V: (c) p_1 and P_1; (d) p_2 and P_2; and (e) p_3 and P_3.

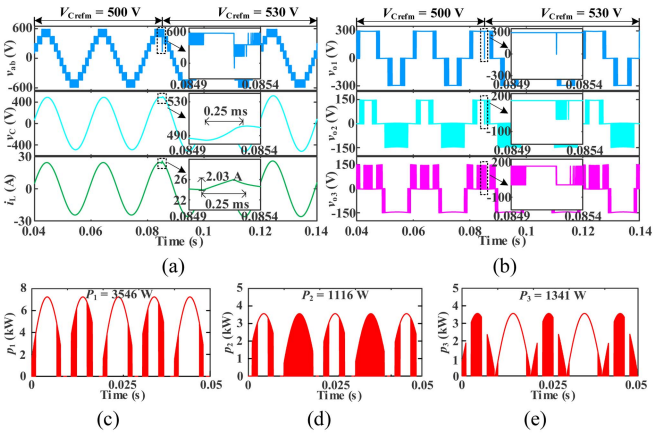

Fig. 15. Simulation results of asymmetric CHBMI under improved FCS-MPC. (a) Waveforms of v_{ab}, v_{C}, and i_{L}. (b) Waveforms of v_{o1}, v_{o2}, v_{o3}. Instantaneous power and average power when $V_{\mathrm{Crefm}} = 500$ V: (c) p_1 and P_1; (d) p_2 and P_2; and (e) p_3 and P_3.

TABLE VIII
STEADY-STATE AND DYNAMIC PERFORMANCE INDICATORS OF ASYMMETRIC CHBMI UNDER DIFFERENT CONTROL METHODS

	Proposed control method	PBIH-PWM-based PI control [14]	Improved FCS-MPC [23]
THD of v_{ab} (V_{Crefm} = 500/530 V)	17.78%/17.23%	17.92%/17.29%	17.52%/17.17%
THD of v_C (V_{Crefm} = 500/530 V)	0.37%/0.33%	0.42%/0.36%	0.31%/0.27%
RMSE of v_C (V_{Crefm} = 500/530 V)	1.2208/1.5651 V	2.6603/3.1159 V	2.3096/ 3.9941 V
RMSE of i_L (V_{Crefm} = 500/530 V)	0.4101/0.6225 A	1.014/1.3132 A	0.9077/0.9985 A
v_{ab} and v_{o1}–v_{o3} have level jumps?	No	No	No
Maximum fluctuation of v_C/i_L	0 V/0 A	20 V/2.76 A	0 V/2.03 A
Dynamic response time	0.2 ms	0.97 ms	0.25 ms
Power balance degree	99.73%	78.29%	45.58%

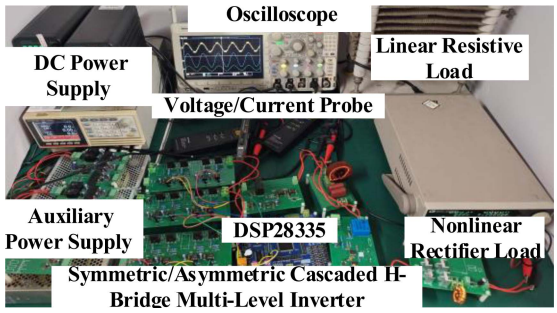

Fig. 16. Experimental platform of symmetric/asymmetric CHBMI with 3 inverter units.

control methods are applied to the asymmetric CHBMI. From the comparative analysis of Table VIII, although the THD of v_{ab} and v_C of the proposed method is slightly higher than that of the improved FCS-MPC, it is less than that of PBIH-PWM-based PI control. Moreover, compared with the other two methods, when V_{Crefm} = 500/530 V with the proposed method applied, the RMSE of v_C and i_L of the asymmetric CHBMI is the lowest, being 1.2208/1.5651 V and 0.4101/0.6225 A, respectively. In addition, when V_{Crefm} changes suddenly, v_C and i_L do not have unexpected fluctuations, and the dynamic response time is the shortest, only 0.2 ms. In terms of power balance, the power balance degree of the proposed method is the highest at 99.73%, significantly better than the other two methods.

Therefore, the analysis of the simulation results shows that, compared with other methods, the proposed method also has comprehensive advantages in terms of steady-state accuracy, dynamic response speed, and power balance for the asymmetric CHBMI.

VI. EXPERIMENTAL VALIDATION

To further experimentally verify the proposed method, an experimental platform of symmetric/asymmetric CHBMI with 3 inverter units (see Fig. 16) was constructed. The switches were SGH40N60, the voltage probe Tektronix P5200A, and the current probe CYBERTEK CP8030H.

A. Experimental Results of Symmetric CHBMI

The experimental parameter settings are shown in Table IX.

According to Section III-B, the control coefficients of the proposed method were set to k_1 = 52 500 and k_2 = 112 500. The control coefficients of PS-PWM-based PI control and CR-LS-PWM-based PI control were designed as k_{pv} = 3, k_{iv} = 200, k_{pc} = 0.8, and k_{ic} = 180. Figs. 17–20 respectively show the experimental results of using the proposed method, PS-PWM-based PI control, CR-LS-PWM-based PI control, and the improved FCS-MPC. During the experiment, the value of V_{Crefm} increased from 250 V to 280 V.

TABLE IX
MAIN EXPERIMENTAL PARAMETERS OF SYMMETRIC CHBMI

Symbol	Parameters	Values
E	DC source voltage	100 V
V_{Crefm}	Amplitude of the reference voltage v_{Cref}	250/280 V
T	Period of the reference voltage v_{Cref}	0.02 s
L	Filter inductor	1 mH
C	Filter capacitor	10 μF
R_L	Resistive load	30 Ω

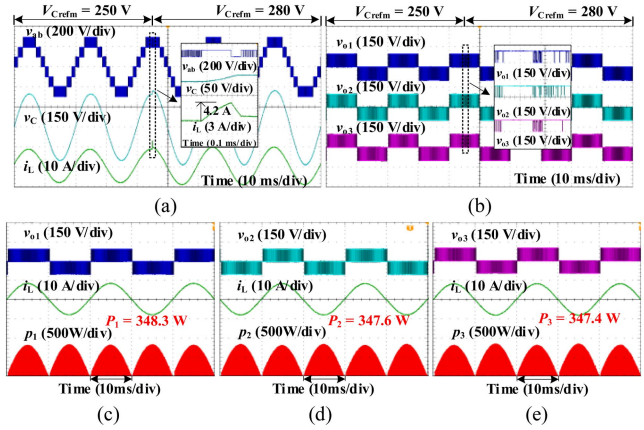

Fig. 17. Experimental results of symmetric CHBMI under the proposed control method. (a) Waveforms of v_{ab}, v_C, and i_L. (b) Waveforms of v_{o1}, v_{o2}, v_{o3}. Instantaneous power and average power when V_{Crefm} = 250 V: (c) p_1 and P_1; (d) p_2 and P_2; and (e) p_3 and P_3.

Table X presents the steady-state, dynamic performance, execution time, power balance degree, and actual efficiency when different control methods are applied to the symmetric CHBMI. Table XI presents the actual switching frequency and switching loss of the symmetric CHBMI when different control methods are applied. As shown in Table X, compared to the other three methods, the proposed method achieves the lowest THD of v_{ab} and v_C when V_{Crefm} = 250/280 V, with values of only 23.91%/20.74% and 0.21%/0.20%, respectively.

Among them, the THD of v_{ab} of the proposed method is reduced by 6.29%−12.24% compared with PS-PWM-based PI

TABLE X
STEADY-STATE AND DYNAMIC PERFORMANCE, EXECUTION TIME, POWER BALANCE DEGREE, AND ACTUAL EFFICIENCY OF SYMMETRIC CHBMI UNDER DIFFERENT CONTROL METHODS

	Proposed control method	PS-PWM-based PI control [10]	CR-LS-PWM-based PI control [13]	Improved FCS-MPC [23]
THD of v_{ab} (V_{Crefm} = 250/280 V)	23.91%/20.74%	36.15%/31.68%	30.20%/29.00%	24.07%/20.92%
THD of v_C (V_{Crefm} = 250/280 V)	0.21%/0.20%	0.57%/0.42%	0.43%/0.36%	0.24%/0.23%
v_{ab} and v_{o1}–v_{o3} have level jumps?	No	Yes	Yes	No
Maximum fluctuation of v_C/i_L	0 V/4.2 A	12 V/6.0 A	20 V/6.6 A	0 V/3.3 A
Dynamic response time	0.15 ms	0.63 ms	0.65 ms	0.18 ms
Execution time	10.32 μs	9.44 μs	11.17 μs	13.23 μs
Power balance degree	99.69%	99.11%	98.51%	–32.75%
Actual efficiency	95.16%	94.75%	94.83%	93.74%

TABLE XI
ACTUAL SWITCHING FREQUENCY AND SWITCHING LOSS OF SYMMETRIC CHBMI UNDER DIFFERENT CONTROL METHODS

	Proposed control method	PS-PWM-based PI control [10]	CR-LS-PWM-based PI control [13]	Improved FCS-MPC [23]
Effective switching frequency of Q_{11}–Q_{12}	15.02 kHz	20.34 kHz	19.99 kHz	20.03 kHz
Switching times/loss of Q_{11}–Q_{12} in a T	300/0.7639 W	408/1.0390 W	399/1.0160 W	402/1.0237 W
Effective switching frequency of Q_{13}–Q_{14}	14.89 kHz	20.24 kHz	19.26 kHz	20.09 kHz
Switching times/loss of Q_{13}–Q_{14} in a T	298/0.7589 W	405/1.0313 W	391/0.9957 W	403/1.0262 W
Effective switching frequency of Q_{21}–Q_{22}	15.19 kHz	20.12 kHz	20.51 kHz	20.53 kHz
Switching times/loss of Q_{21}–Q_{22} in a T	305/0.7767 W	403/1.0262 W	412/1.0491 W	410/1.0441 W
Effective switching frequency of Q_{23}–Q_{24}	15.02 kHz	20.04 kHz	20.50 kHz	20.50 kHz
Switching times/loss of Q_{23}–Q_{24} in a T	301/0.7665 W	401/1.0211 W	410/1.0441 W	410/1.0441 W
Effective switching frequency of Q_{31}–Q_{32}	15.01 kHz	20.11 kHz	19.29 kHz	20.21 kHz
Switching times/loss of Q_{31}–Q_{32} in a T	299/0.7614 W	404/1.0288 W	387/0.9855 W	406/1.0339 W
Effective switching frequency of Q_{33}–Q_{34}	15.08 kHz	20.07 kHz	20.14 kHz	20.53 kHz
Switching times/loss of Q_{33}–Q_{34} in a T	303/0.7716 W	403/1.0262 W	405/1.0313 W	411/1.0466 W
Total switching loss in a T	9.1979 W	12.3453 W	12.2435 W	12.4370 W

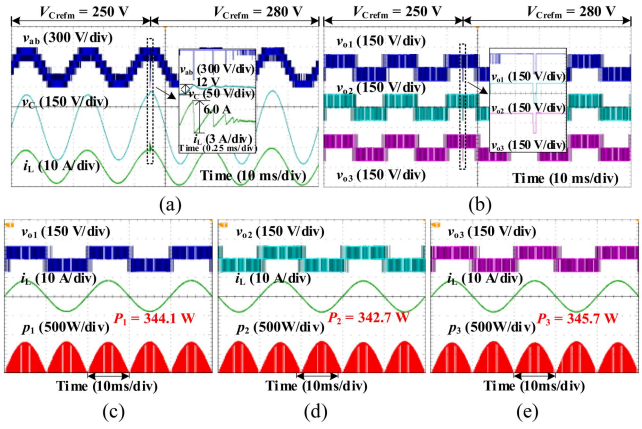

Fig. 18. Experimental results of symmetric CHBMI under PS-PWM-based PI control. (a) Waveforms of v_{ab}, v_C, and i_L. (b) Waveforms of v_{o1}, v_{o2}, v_{o3}. Instantaneous power and average power when $V_{Crefm} = 250$ V: (c) p_1 and P_1; (d) p_2 and P_2; and (e) p_3 and P_3.

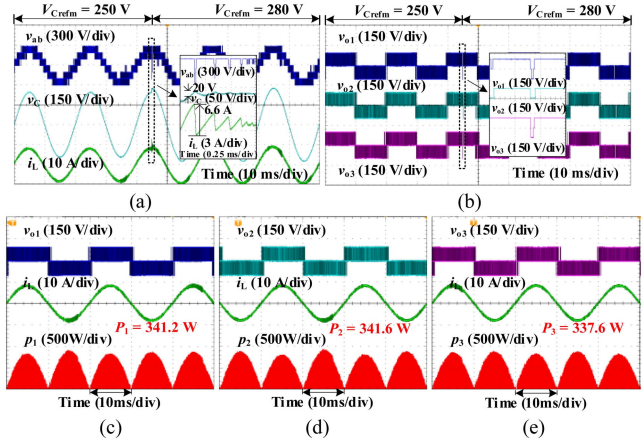

Fig. 19. Experimental results of symmetric CHBMI under CR-LS-PWM-based PI control. (a) Waveforms of v_{ab}, v_C, and i_L. (b) Waveforms of v_{o1}, v_{o2}, v_{o3}. Instantaneous power and average power when $V_{Crefm} = 250$ V: (c) p_1 and P_1; (d) p_2 and P_2; and (e) p_3 and P_3.

control and CR-LS-PWM-based PI control. And when V_{Crefm} changes suddenly, there is no level jump in v_{ab} and $v_{o1}-v_{o3}$ of the proposed method, while there are jumps in PS-PWM-based PI control and CR-LS-PWM-based PI control. Although the maximum fluctuation value of i_L of the proposed method is slightly higher than that of the improved FCS-MPC, its dynamic response time is the shortest, only 0.15 ms. Compared with PS-PWM-based PI control and CR-LS-PWM-based PI control, the dynamic response time of the proposed method is shortened by 76.19% and 76.92%, respectively. In addition, although the execution time of the proposed method is slightly higher than that of PS-PWM-based PI control, the power balance degree and actual efficiency are the highest, 99.69% and 95.16%, respectively. Among them, the power balance degree is increased by 132.44% compared with the improved FCS-MPC. From the comparative analysis of Table XI, the actual switching frequency of the proposed method is the lowest, and the switching loss is the smallest.

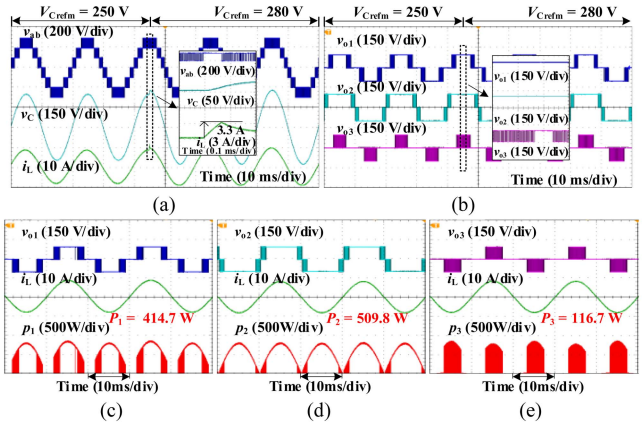

Fig. 20. Experimental results of symmetric CHBMI under improved FCS-MPC. (a) Waveforms of v_{ab}, v_C, and i_L. (b) Waveforms of v_{o1}, v_{o2}, v_{o3}. Instantaneous power and average power when V_{Crefm} = 250 V: (c) p_1 and P_1; (d) p_2 and P_2; and (e) p_3 and P_3.

TABLE XII
MAIN EXPERIMENTAL PARAMETERS OF ASYMMETRIC CHBMI

Symbol	Parameters	Values
mE	DC-side voltage value of high-voltage unit 1	144 V
E	DC-side voltage value of low-voltage units 2–3	72 V
V_{Crefm}	Amplitude of the reference voltage v_{Cref}	220/250 V
T	Period of the reference voltage v_{Cref}	0.02 s
L	Filter inductor	10 mH
C	Filter capacitor	10 μF
L_r	Filter inductor	0.2 mH
C_r	Filter capacitor	1 μF
R	Resistive load	20 Ω

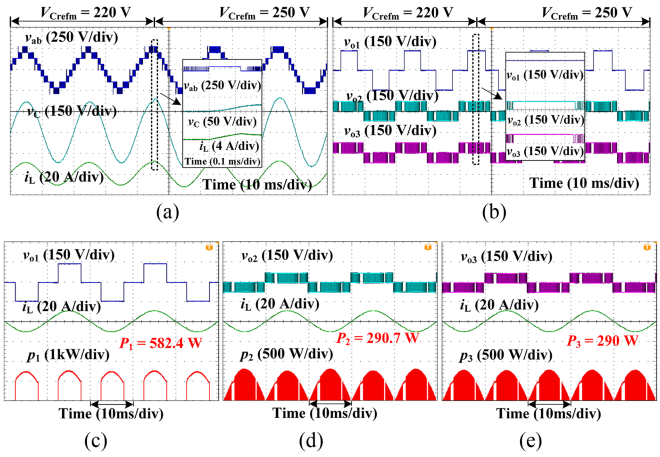

Fig. 21. Experimental results of asymmetric CHBMI under the proposed control method. (a) Waveforms of v_{ab}, v_C, and i_L. (b) Waveforms of v_{o1}, v_{o2}, v_{o3}. Instantaneous power and average power when V_{Crefm} = 220 V: (c) p_1 and P_1; (d) p_2 and P_2; and (e) p_3 and P_3.

B. Experimental Results of Asymmetric CHBMI

The experimental parameter settings are shown in Table XII. According to Section III-B, the control coefficients of the proposed method were set to k_1 = 272 500 and k_2 = 151 300, and the control coefficients of PBIH-PWM-based PI control were designed as k_{pv} = 2.5, k_{iv} = 350, k_{pc} = 1.2, and k_{ic} = 220. Figs. 21–23 respectively show the experimental results of using the proposed method, PBIH-PWM-based PI control, and

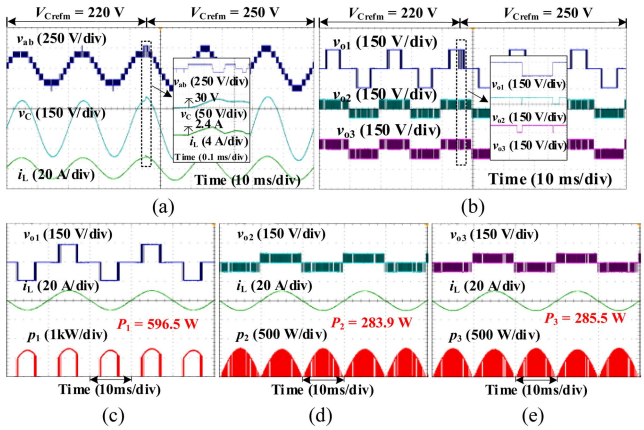

Fig. 22. Experimental results of asymmetric CHBMI under PBIH-PWM-based PI control. (a) Waveforms of v_{ab}, v_C, and i_L. (b) Waveforms of v_{o1}, v_{o2}, v_{o3}. Instantaneous power and average power when V_{Crefm} = 220 V: (c) p_1 and P_1; (d) p_2 and P_2; and (e) p_3 and P_3.

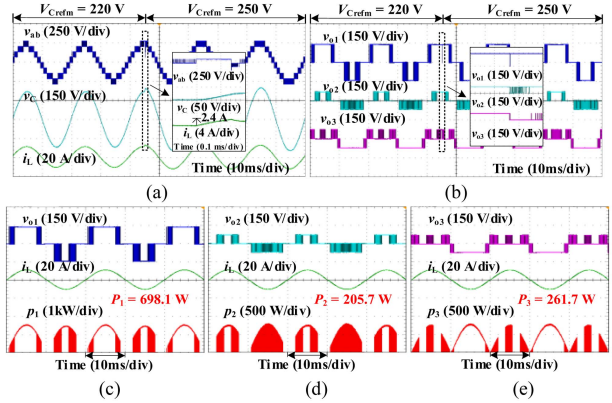

Fig. 23. Experimental results of asymmetric CHBMI under improved FCS-MPC. (a) Waveforms of v_{ab}, v_C, and i_L. (b) Waveforms of v_{o1}, v_{o2}, v_{o3}. Instantaneous power and average power when V_{Crefm} = 220 V: (c) p_1 and P_1; (d) p_2 and P_2; and (e) p_3 and P_3.

the improved FCS-MPC. During the experiment, the value of V_{Crefm} increased from 220 to 250 V.

Table XIII presents the steady-state, dynamic performance, execution time, power balance degree, and actual efficiency when different control methods are applied to the asymmetric CHBMI. Table XIV presents the actual switching frequency and switching loss of the asymmetric CHBMI when different control methods are applied. From the comparative analysis of Table XIII, the THD of v_{ab} and v_C of the proposed method is slightly higher than that of the improved FCS-MPC but lower than that of PBIH-PWM-based PI control. When V_{Crefm} changes suddenly, there is no unexpected fluctuation in v_C and i_L of the proposed method. The v_C of the improved FCS-MPC also has no fluctuation, but its maximum fluctuation value of i_L is 2.4 A. The maximum fluctuation values of v_C and i_L of PBIH-PWM-based PI control are 30 V and 2.4 A, respectively. Moreover, the dynamic response time of the proposed method is the lowest, only 0.12 ms. Compared with the improved FCS-MPC and PBIH-PWM-based PI control, the dynamic response time of the proposed method is shortened by 25% and 68.42% respectively. Although the execution time of the proposed method is slightly higher than that of PBIH-PWM-based PI control, its power

TABLE XIII
STEADY-STATE AND DYNAMIC PERFORMANCE, EXECUTION TIME, POWER BALANCE DEGREE, AND ACTUAL EFFICIENCY OF ASYMMETRIC CHBMI UNDER DIFFERENT CONTROL METHODS

	Proposed control method	PBIH-PWM-based PI control [14]	Improved FCS-MPC [23]
THD of v_{ab} (V_{Crefm} = 220/250 V)	22.37%/21.35%	22.57%/21.44%	20.67%/20.14%
THD of v_C (V_{Crefm} = 220/250 V)	0.22%/0.20%	0.26%/0.22%	0.18%/0.13%
v_{ab} and v_{o1}–v_{o3} have level jumps?	No	No	No
Maximum fluctuation of v_C/i_L	0 V/0 A	30 V/2.4 A	0 V/2.4 A
Dynamic response time	0.12 ms	0.38 ms	0.16 ms
Execution time	11.18 μs	10.54 μs	13.47 μs
Power balance degree	99.56%	93.03%	40.62%
Actual efficiency	95.78%	94.17%	93.41%

TABLE XIV
ACTUAL SWITCHING FREQUENCY AND SWITCHING LOSS OF ASYMMETRIC CHBMI UNDER DIFFERENT CONTROL METHODS

	Proposed control method	PBIH-PWM-based PI control [14]	Improved FCS-MPC [23]
Effective switching frequency of Q_{11}–Q_{12}	50 Hz	391 Hz	20.67 kHz
Switching times/loss of Q_{11}–Q_{12} in a T	1/0.0025 W	8/0.0204 W	414/1.0542 W
Effective switching frequency of Q_{13}–Q_{14}	50 Hz	349 Hz	20.47 kHz
Switching times/loss of Q_{13}–Q_{14} in a T	1/0.0025 W	6/0.0153 W	411/1.0466 W
High-voltage unit operating at 50 Hz?	Yes	No	No
Effective switching frequency of Q_{21}–Q_{22}	14.47 kHz	19.95 kHz	20.89 kHz
Switching times/loss of Q_{21}–Q_{22} in a T	291/0.7410 W	400/1.0186 W	418/1.0644 W
Effective switching frequency of Q_{23}–Q_{24}	14.26 kHz	19.58 kHz	20.64 kHz
Switching times/loss of Q_{23}–Q_{24} in a T	287/0.7308 W	392/0.9982 W	413/1.0517 W
Effective switching frequency of Q_{31}–Q_{32}	11.98 kHz	20.02 kHz	20.48 kHz
Switching times/loss of Q_{31}–Q_{32} in a T	241/ 0.6137 W	401/1.0211 W	411/1.0466 W
Effective switching frequency of Q_{33}–Q_{34}	12.34 kHz	19.91 kHz	19.90 kHz
Switching times/loss of Q_{33}–Q_{34} in a T	251/0.6392 W	400/1.0186 W	399/1.0160 W
Total switching loss in a T	5.4597 W	8.1844 W	12.5592 W

balance degree and actual efficiency are the highest, 99.56% and 95.78%, respectively. Among them, the power balance degree is increased by 58.94% and 6.53% compared with the improved FCS-MPC and PBIH-PWM-based PI control, respectively. From the comparative analysis of Table XIV, compared with the other two methods, the actual switching frequency of the proposed method is the lowest, the switching loss is the smallest, and it ensures that the high-voltage unit always operates at the fundamental frequency.

Therefore, the experimental results shown in Figs. 17–23 are consistent with the simulation results shown in Figs. 9–15. The results show that, whether for the symmetric CHBMI with a linear load or the asymmetric CHBMI with a nonlinear load, the proposed method has comprehensive advantages compared to other methods in terms of steady-state accuracy, dynamic response speed, power balance, and switching loss. Moreover, the proposed method can also ensure that the high-voltage inverter unit of the asymmetric CHBMI operates at the fundamental frequency.

VII. CONCLUSION

To achieve power balance in CHBMIs while ensuring good steady-state and dynamic performance, this article proposes a feedback linearization random selection control method based on the sigmoid function. The proposed method is applicable to symmetric and asymmetric CHBMIs with any number of inverter units, which are connected with linear or nonlinear loads. Simulations and experiments were carried out on a symmetric cascaded H-bridge 7-level inverter with a linear resistive load and an asymmetric cascaded H-bridge 9-level inverter with a nonlinear rectifier load, and comparisons were made with other methods. The results show that:

1) For the symmetric CHBMI, compared with PS-PWM-based PI control and CR-LS-PWM-based PI control, the THD of the output level using the proposed method is reduced by 6.29%–12.24%. Moreover, when the maximum amplitude of the reference voltage changes suddenly, there is no level jump in the output level using the proposed method. However, both PS-PWM-based PI control and CR-LS-PWM-based PI control have level jumps. In addition, compared with these two methods, the dynamic response time of the proposed method is shortened by 76.19% and 76.92% respectively. In terms of power balance degree, the proposed method is improved by 132.44% compared with the improved FCS-MPC.
2) For the asymmetric CHBMI, the THD of the output level using the proposed method is slightly higher than that of the improved FCS-MPC, but lower than that of PBIH-PWM-based PI control. Compared with these two methods, the dynamic response time of the proposed method is shortened by 25% and 68.42% respectively, and the power balance degree is increased by 58.94% and 6.53% respectively. In addition, compared to these two methods that struggle to ensure the high-voltage unit works in a low-frequency state, the proposed method can ensure that the high-voltage unit operates at the fundamental frequency, thereby effectively reducing the loss of switches.

Therefore, compared with the existing methods, the proposed method achieves better steady-state and dynamic performance, and a higher power balance degree.

REFERENCES

[1] S. Kouro et al., "Recent advances and industrial applications of multilevel converters," *IEEE Trans. Ind. Electron.*, vol. 57, no. 8, pp. 2553–2580, Aug. 2010, doi: 10.1109/TIE.2010.2049719.

[2] M. A. Perez, S. Ceballos, G. Konstantinou, J. Pou, and R. P. Aguilera, "Modular multilevel converters: Recent achievements and challenges," *IEEE Open J. Ind. Electron. Soc.*, vol. 2, pp. 224–239, Feb. 2021, doi: 10.1109/OJIES.2021.3060791.

[3] R. Vasu, S. K. Chattopadhyay, and C. Chakraborty, "Asymmetric cascaded H-bridge multilevel inverter with single DC source per phase," *IEEE Trans. Ind. Electron.*, vol. 67, no. 7, pp. 5398–5409, Jul. 2020, doi: 10.1109/TIE.2019.2934080.

[4] H. Yao, Y. Yan, Y. Cao, P. Song, and T. Shi, "A variable duty cycle-based predictive control for PMSM fed by cascaded H-bridge inverter," *IEEE J. Emerg. Sel. Topics Power Electron.*, vol. 10, no. 4, pp. 4195–4206, Aug. 2022, doi: 10.1109/JESTPE.2022.3154045.

[5] I. Gunsal, D. Stone, and M. Foster, "Suppressing leakage current for cascaded H-bridge inverters in renewable energy and storage systems," *IEEE Trans. Ind. Electron.*, vol. 68, no. 11, pp. 11035–11043, Nov. 2021, doi: 10.1109/TIE.2020.3031524.

[6] R. Sharma and A. Das, "Extended reactive power exchange with faulty cells in grid-tied cascaded H-bridge converter for solar photovoltaic application," *IEEE Trans. Power Electron.*, vol. 35, no. 6, pp. 5683–5691, Jun. 2020, doi: 10.1109/TPEL.2019.2950336.

[7] P. Lingom, J. Song-Manguelle, D. Mon-Nzongo, R. Flesch, and T. Jin, "Analysis and control of PV cascaded H-bridge multilevel inverter with failed cells and changing meteorological conditions," *IEEE Trans. Power Electron.*, vol. 36, no. 2, pp. 1777–1789, Feb. 2021, doi: 10.1109/TPEL.2020.3009107.

[8] S. Yang et al., "Quantitative comparison and analysis of different power routing methods for single-phase cascaded H-bridge photovoltaic grid-connected inverter," *IEEE Trans. Power Electron.*, vol. 36, no. 4, pp. 4134–4152, Apr. 2021, doi: 10.1109/TPEL.2020.3024282.

[9] J. Rodriguez, J.-S. Lai, and F. Z. Peng, "Multilevel inverters: A survey of topologies, controls, and applications," *IEEE Trans. Ind. Electron.*, vol. 49, no. 4, pp. 724–738, Aug. 2002, doi: 10.1109/TIE.2002.801052.

[10] M. Hagiwara and H. Akagi, "Control and experiment of pulsewidth modulated modular multilevel converters," *IEEE Trans. Power Electron.*, vol. 24, no. 7, pp. 1737–1746, Jul. 2009, doi: 10.1109/TPEL.2009.2014236.

[11] M. Vasiladiotis, N. Cherix, and A. Rufer, "Accurate capacitor voltage ripple estimation and current control considerations for grid-connected modular multilevel converters," *IEEE Trans. Power Electron.*, vol. 29, no. 9, pp. 4568–4579, Sep. 2014, doi: 10.1109/TPEL.2013.2286293.

[12] Y. Li, Y. Wang, and B. Q. Li, "Generalized theory of phase-shifted carrier PWM for cascaded H-bridge converters and modular multilevel converters," *IEEE J. Emerg. Sel. Topics Power Electron.*, vol. 4, no. 2, pp. 589–605, Jun. 2016, doi: 10.1109/JESTPE.2015.2476699.

[13] M. Meraj, S. Rahman, A. Iqbal, and N. Al Emadi, "Novel level shifted PWM technique for unequal and equal power sharing in quasi Z-source cascaded multilevel inverter for PV systems," *IEEE J. Emerg. Sel. Topics Power Electron.*, vol. 9, no. 1, pp. 937–948, Feb. 2021, doi: 10.1109/JESTPE.2019.2952206.

[14] M. Ye, R. Peng, Z. Tong, Z. Chen, and Z. Miao, "A generalized scheme with linear power balance and uniform switching loss for asymmetric cascaded H-bridge multilevel inverters," *IEEE Trans. Power Electron.*, vol. 37, no. 3, pp. 2719–2730, Mar. 2022, doi: 10.1109/TPEL.2021.3114369.

[15] R. Sarker, A. Datta, and S. Debnath, "FPGA implementation of phase disposition PWM (PD-PWM) strategy for cascaded H-bridge multilevel inverter (CHB-MLI)," in *Proc. IEEE Appl. Signal Process. Conf.*, 2020, pp. 80–84, doi: 10.1109/ASPCON49795.2020.9276676.

[16] S. Vazquez, J. Rodriguez, M. Rivera, L. Franquelo, and M. Norambuena, "Model predictive control for power converters and drives: Advances and trends," *IEEE Trans. Ind. Electron.*, vol. 64, no. 2, pp. 935–947, Feb. 2017, doi: 10.1109/TIE.2016.2625238.

[17] T. He, M. Wu, R. P. Aguilera, D. D.-C. Lu, Q. Liu, and S. Vazquez, "Low computational burden model predictive control for single-phase cascaded H-bridge converters without weighting factor," *IEEE Trans. Ind. Electron.*, vol. 70, no. 3, pp. 2396–2406, Mar. 2023, doi: 10.1109/TIE.2022.3167133.

[18] F. Simonetti, A. D'Innocenzo, and C. Cecati, "Simple explicit solution of finite control set model predictive control for cascaded H-bridge inverters," *IEEE Trans. Ind. Electron.*, vol. 71, no. 8, pp. 9620–9630, Aug. 2024, doi: 10.1109/TIE.2023.3321979.

[19] P. Cortés, A. Wilson, S. Kouro, J. Rodriguez, and H. Abu-Rub, "Model predictive control of multilevel cascaded H-bridge inverters," *IEEE Trans. Ind. Electron.*, vol. 57, no. 8, pp. 2691–2699, Aug. 2010, doi: 10.1109/TIE.2010.2041733.

[20] B. Gutierrez and S. Kwak, "Modular multilevel converters (MMCs) controlled by model predictive control with reduced calculation burden," *IEEE Trans. Power Electron.*, vol. 33, no. 11, pp. 9176–9187, Nov. 2018, doi: 10.1109/TPEL.2018.2789455.

[21] Z. Ni et al., "A new MPC formulation based on suboptimal voltage vectors for multilevel inverters," *IEEE J. Emerg. Sel. Topics Power Electron.*, vol. 10, no. 6, pp. 7261–7270, Dec. 2022, doi: 10.1109/JESTPE.2022.3200063.

[22] I. Kim, R. Chan, and S. Kwak, "Model predictive control method for CHB multi-level inverter with reduced calculation complexity and fast dynamics," *IET Elect. Power Appl.*, vol. 11, no. 5, pp. 784–792, May 2017, doi: 10.1049/iet-epa.2016.0330.

[23] I. Harbi et al., "Model-predictive control of multilevel inverters: Challenges, recent advances, and trends," *IEEE Trans. Power Electron.*, vol. 38, no. 9, pp. 10845–10868, Sep. 2023, doi: 10.1109/TPEL.2023.3288499.

[24] Y. Lu, X. Huang, Y. Huang, and D. Liu, "Sigmoid function model for a PFM power electronic converter," *IEEE Trans. Power Electron.*, vol. 35, no. 4, pp. 4233–4241, Apr. 2020, doi: 10.1109/TPEL.2019.2935632.

[25] Y. Lu, X. Wei, X. Huang, and Z. Yin, "Memristive characteristics and extreme multistability of LLC DC-DC resonant converters," *IEEE Trans. Ind. Electron.*, vol. 71, no. 7, pp. 7020–7029, Jul. 2024, doi: 10.1109/TIE.2023.3299053.

[26] J. Adamy, *Nonlinear Systems and Controls*. Berlin, Germany: Springer, 2022, pp. 356–392.

[27] J. Li, H. Pan, X. Long, and B. Liu, "Objective holographic feedbacks linearization control for boost converter with constant power load," *Int. J. Elect. Power Energy Syst.*, vol. 134, Jul. 2022, Art. no. 107310, doi: 10.1016/j.ijepes.2021.107310.

[28] D. Lathrop, *Nonlinear Dynamics and Chaos: With Applications to Physics, Biology, Chemistry, and Engineering*. Boulder, CO, USA: Westview Press, 2015, p. 179.

[29] S. Bacha, I. Munteanu, and A. I. Bratcu, *Power Electronic Converters Modeling and Control: With Case Studies* (ser. Advanced Textbooks in Control and Signal Processing). London, U.K.: Springer, 2013, pp. 140–182.

Zhihong Yin was born in Shaoyang, China, in 1996. He received the B.S. degree in electrical engineering and automation from the Hunan University of Science and Technology, Xiangtan, China, in 2017, and the M.S. degree in electrical engineering from Guangxi University, Nanning, China, in 2021. He is currently working toward the Ph.D. degree in electrical engineering in Guangxi University, Nanning, China.

His research interests include the modeling, analysis, and control of power electronic converters.

Yimin Lu (Member, IEEE) received the B.S. degree in measurement technology and instrumentation from Southeast University, Nanjing, China, in 1992, the M.S. degree in control theory and control engineering from Guangxi University, Nanning, China, in 2000, and the Ph.D. degree in control theory and control engineering from the South China University of Technology, Guangzhou, China, in 2004.

Since 1992, she has been with the School of Electrical Engineering, Guangxi University, where she has been a Professor since 2007. From 2007 to 2008, she was a Postdoctoral Researcher with the Department of Electronic and Electrical Engineering, University of Sheffield, Sheffield, U.K. From 2014 to 2015, she was a Visiting Research Scholar with the Department of Mechanical Engineering and WEMPEC, University of Wisconsin-Madison, Madison, WI, USA. Her current research interests include control theory and its applications in power electronics.